Stratification Breakdown in Antarctic Coastal Polynyas, Part II: Influence of an Ice Tongue and Coastline Geometry

Yilang Xu,[a,b] Weifeng (Gordon) Zhang,[a] Ted Maksym,[a] Rubao Ji,[c] and Yun Li[d]

[a] *Applied Ocean Physics and Engineering Department, Woods Hole Oceanographic Institution, Woods Hole, Massachusetts*

[b] *MIT-WHOI Joint Program in Oceanography/Applied Ocean Science and Engineering, Cambridge, Massachusetts*

[c] *Biology Department, Woods Hole Oceanographic Institution, Woods Hole, Massachusetts*

[d] *School of Marine Science and Policy, University of Delaware, Lewes, Delaware*

Corresponding author: Yilang Xu, yilangxu@mit.edu

14   ABSTRACT

15   This is Part II of a study examining wintertime destratification in Antarctic coastal

16   polynyas, focusing on providing a qualitative description of the influence of ice tongues and

17   headlands, both common geometric features neighboring the polynyas. The model of a coastal

18   polynya used in Part I is modified to include an ice tongue and a headland to investigate their

19   impacts on the dispersal of water formed at the polynya surface, which is referred to as Polynya

20   Source Water (PSW) here. The model configuration qualitatively represents the settings of some

21   coastal polynyas, such as the Terra Nova Bay Polynya. The simulations highlight that an ice tongue

22   next to a polynya tends to break the alongshore symmetry in the lateral return flows toward the

23   polynya, creating a stagnant region in the corner between the ice tongue and polynya where

24   outflow of the PSW in the water column is suppressed. This enhances sinking of the PSW and

25   accelerates destratification of the polynya water column. Adding a headland to the other side of

26   the polynya tends to restore the alongshore symmetry in the lateral return flows, which increases

27   the offshore PSW transport and slows down destratification in the polynya. This work stresses the

28   importance of resolving small-scale geometric features in simulating vertical mixing in the

29   polynya. It provides a framework to explain spatial and temporal variability in rates of

30   destratification and Dense Shelf Water formation across Antarctic coastal polynyas, and helps

31   understand why some polynyas are sources of Antarctic Bottom Water while other are not.

32

1. Introduction

34   Antarctic coastal polynyas are sites of strong wintertime vertical mixing due to sea ice

35   formation and brine rejection (Morales Maqueda et al. 2004). Coastal polynyas are complex

36   systems and can vary drastically in their water-column destratification process (Aoki et al. 2020;

37   Silvano et al. 2018). Destratification of the polynya water column is directly affected by changes

38   in local atmospheric and oceanic forcings (Ackley et al. 2020; Le Bel et al. 2021). Investigating

39   the impacts of these local forcings is vital to understanding the variability in timing and rate of the

40   polynya destratification. Part I of this study (Xu et al. 2023) uses numerical simulations of an

41   idealized Antarctic coastal polynya to investigate the influence of various physical factors on the

42   polynya destratification process. It shows that wind-driven ocean currents can alter lateral dispersal

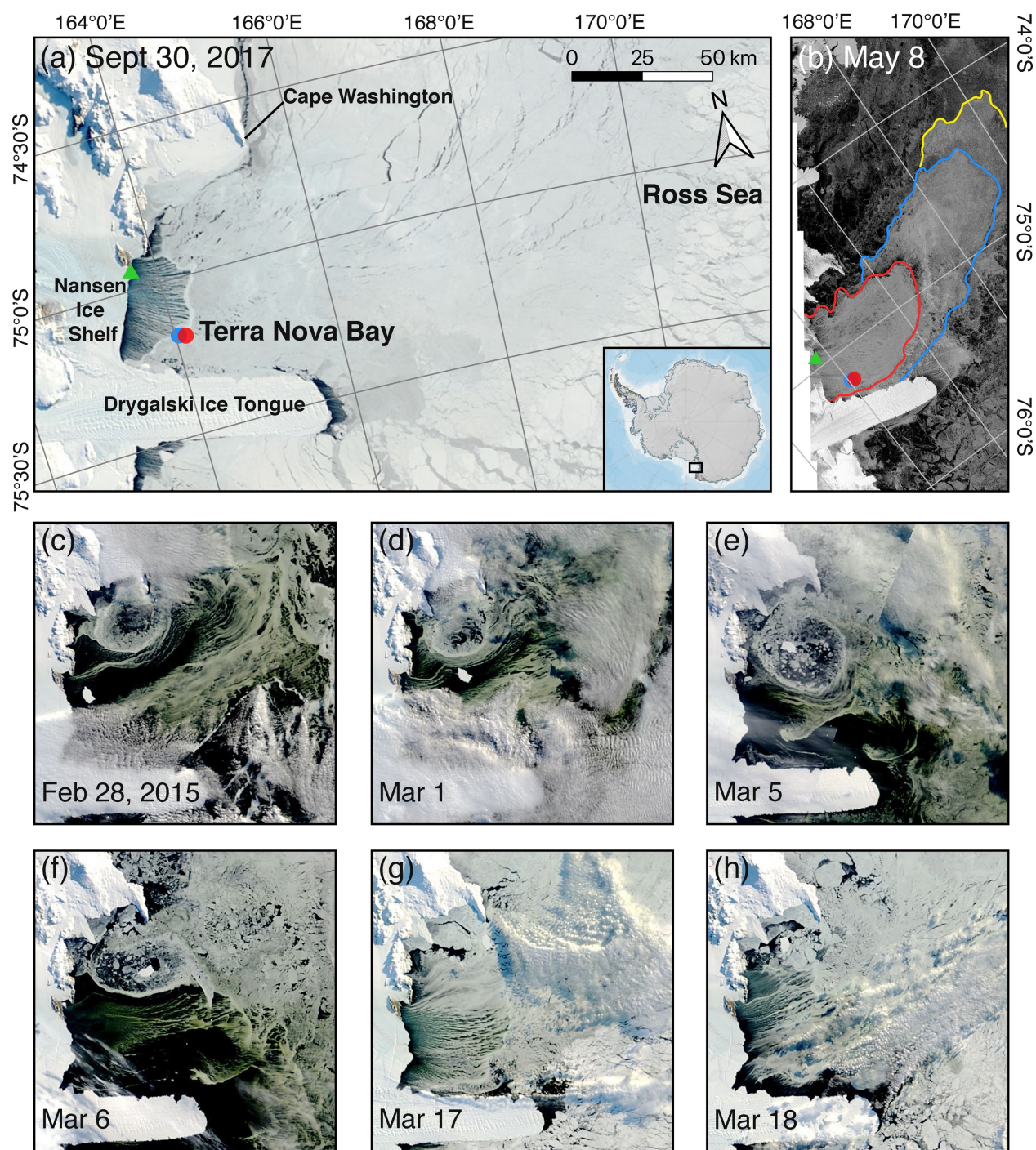43   of the water mass formed at the polynya surface — which we named Polynya Source Water (PSW)

44 — in the water column and affect the strength of vertical mixing in the polynya. In particular,
45 offshore katabatic winds can drive an offshore ocean current, which transports the PSW away from
46 the polynya before it reaches the bottom and thus reduces the polynya destratification rate. In
47 contrast, the alongshore easterly winds can induce onshore Ekman transport, which suppresses the
48 offshore transport of the PSW and enhances vertical mixing in the polynya. Part of the PSW that
49 is dense enough to sink to the bottom becomes Dense Shelf Water (DSW), which flows offshore
50 into the deeper ocean and contributes to the formation of Antarctic Bottom Water (AABW) (Kitade
51 et al. 2014; Ohshima et al. 2013).

52   The Part I study does not consider the influence of other factors, such as ice tongues,
53 coastline geometry, seafloor topography, and the intrusion of Circumpolar Deep Water. Many
54 Antarctic coastal polynyas are accompanied by ice tongues located to the immediate east or
55 southeast of the polynya (Nihashi and Ohshima 2015) and complex seafloor topography (e.g.,
56 Randall-Goodwin et al. 2015; Snow et al. 2018; Yoon et al. 2020). The neighboring ice tongues
57 block the along-coast drift of sea ice into the polynya and help keep the polynyas open (Bromwich
58 and Kurtz 1984; Kurtz and Bromwich 1985; Massom et al. 1998; 2001). Several ice-tongue-
59 associated polynyas have been identified as sources of AABW, e.g., the Cape Darnley Polynya
60 (Ohshima et al. 2013), the Mertz Polynya (Williams et al. 2010), and the Terra Nova Bay Polynya
61 (e.g., Budillon and Spezie 2000; Rusciano et al. 2013). Some of these studies suggest that AABW
62 formation in these polynyas is subject to the impact of the ice tongues. Consequently, changes in
63 the ice tongues morphology (e.g., length) may alter the AABW production. One example is the
64 calving of the Mertz Glacier Tongue in 2010, which greatly reduced the sea ice productivity in the
65 Mertz Polynya (Tamura et al. 2012). A reduction in AABW formation was observed in the Mertz
66 Polynya region two years after the calving event (Lacarra et al. 2014; Snow et al. 2018). The length
67 of the Mertz Glacier Tongue changes periodically, and multiple calving events have occurred in
68 the past (Giles 2017). This suggests that the sea ice and DSW formation in the Mertz Polynya
69 region may also vary in time following changes in the Mertz Glacier Tongue. Since the Mertz
70 Glacier Tongue is currently growing at a rate of ~1 km per year (Giles 2017), a gradual variation
71 of the Mertz Polynya activity is expected in the next several decades with growth of the Mertz
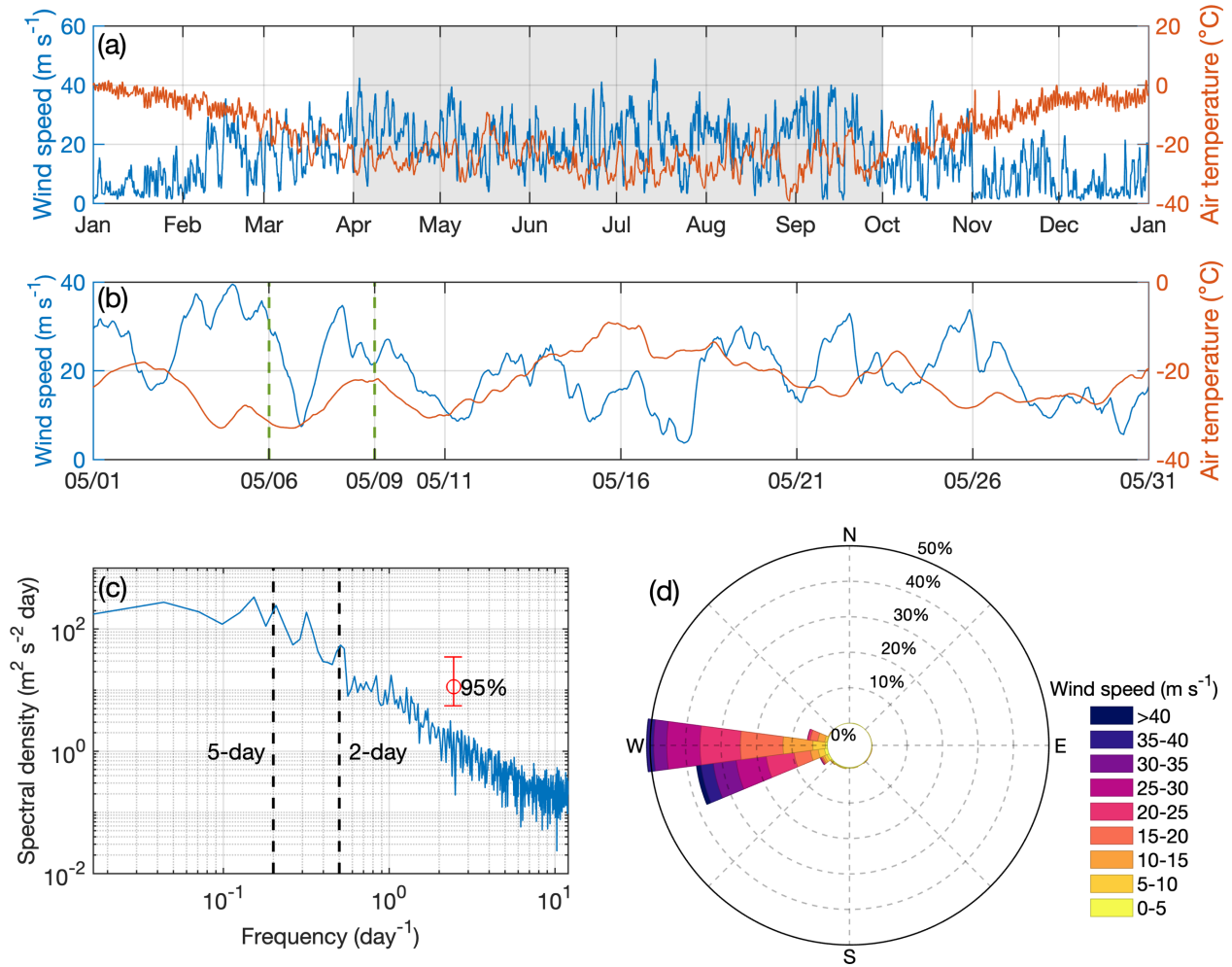72 Glacier Tongue.

73   This Part II study focuses on two influencing factors that are not considered in Part I, ice
74 tongue and coastline geometry, and investigates their influence on the destratification process in

75   Antarctic coastal polynyas. Previous studies (Kurtz and Bromwich 1985; Ohshima et al. 2013;

76   Williams et al. 2010) of the influence of ice tongues on the PSW formation mainly consider the

77   blocking effect of an ice tongue on the advection of sea ice into the polynya, which prolongs the

78   duration of polynya opening and enhances brine rejection at the surface. Since ice tongues are

79   hundreds of meters thick (Stevens et al. 2017), the blocking effect presumably extends deep into

80   the water column and affects the subsurface ocean current in the polynya region. Consequently,

81   PSW circulation in the polynya region may be altered, which, as demonstrated in Part I, could

82   change the destratification rate in the polynya water column. Besides ice tongues, coastline

83   geometry in the vicinity of Antarctic coastal polynyas is usually complex (Nihashi and Ohshima

84   2015), which might also influence the PSW circulation and destratification process. Because of

85   their small spatial scales, ice tongue and local coastline geometry are often not fully resolved in

86   large-scale ocean models (e.g., Dinniman et al. 2020) and details of their impacts on PSW

87   circulation are largely unknown.

88   In this work, the Terra Nova Bay Polynya (TNBP; Fig. 1a) is used as a representative

89   example to illustrate the need to consider the influence of ice tongues and coastline geometry,

90   particularly, a neighboring headland, in the analysis of polynya wintertime destratification and

91   PSW circulation. The TNBP is located in the western Ross Sea, between the Drygalski Ice Tongue

92   to the south and a headland named Cape Washington to the north. Similar to the Mertz Glacier

93   Tongue, the length of the Drygalski Ice Tongue has also changed in the past century due to calving

94   events (Frezzotti and Mabin 1994; Parmiggiani and Fragiacomo 2005). During the winter months

95   (April–September), air temperature in this region frequently drops below -20 °C (Fig. 2a), and

96   strong katabatic winds from the Nansen Ice Shelf blow offshore (eastward; Fig. 2d), extending

97   beyond the Terra Nova Bay (Bromwich 1989; Wenta and Cassano 2020) and forming the TNBP.

98   The TNBP is characterized by strong sea ice production and DSW formation in winter (Budillon

99   and Spezie 2000; Rusciano et al. 2013). It is sustained by katabatic winds and the Drygalski Ice

100 Tongue, which intrudes ~90 km into the Ross Sea (Indrigo et al. 2020), and blocks sea ice from

101 entering the TNBP from the south (Kurtz and Bromwich 1985).

102

Fig. 1. (a) Terra/Aqua MODIS satellite image of the Terra Nova Bay Polynya region on 30 September, 2017. (b) Sentinel-1 SAR satellite image of the Terra Nova Bay Polynya on May 8, 2017. In both (a) and (b), the green triangle locates the Manuela weather station; the blue and red circles denote the locations of PIPERS CTD casts on May 6 and 9, 2017, respectively. Colored lines in (b) outline the offshore boundary of the polynya and outer boundaries of the previous sea ice plume. These images are selected to show a clear (cloud-free) pattern of the polynya surface and its offshore sea ice plume. (c-h) Terra/Aqua MODIS satellite images of the Terra Nova Bay Polynya between 28 February and 18 March, 2015.
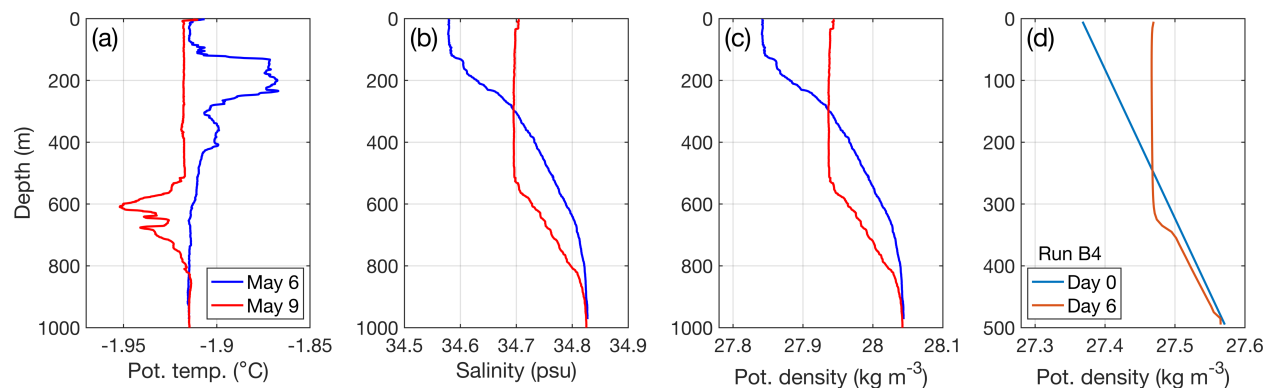
Fig. 2. (a-b) Wind speed and air temperature measured at the Manuela weather station in 2017; (b) is a zoomed-in version of (a) showing the time series in May; (c) spectral density of the measured wind speed; (d) wind rose plots of the wind speed and the direction it comes from in the winter months (April–September). The grey shade in (a) highlights the austral winter months; the green dashed lines in (b) highlight the times of PIPERS CTD casts; the error bar in (c) indicates the 95% confidence interval; dashed lines in (c) denote frequencies corresponding to oscillation periods of 2 and 5 days.

In May 2017, during the *Polynyas, Ice Production and seasonal Evolution in the Ross Sea* (PIPERS) project field campaign (Ackley et al. 2020), researchers observed a rapid deepening of the surface mixed layer in the TNBP (Thompson et al. 2020). Conductivity-Temperature-Density (CTD) cast in the vicinity of the ice tongue on May 6 showed that the water column was stratified below 100 m (Fig. 3). On May 9, another CTD cast at the same location showed that temperature and salinity in the upper 500 m had been largely homogenized (Fig. 3). Hence, within three days, the depth of the surface mixed layer had extended from 100 m to 500 m. This mixing event took place much faster than the gradual mixing in the Vincennes Bay Polynya, which usually takes

several months as revealed by the seal data in Part I. The atmospheric data from Manuela Automatic Weather Station on the coast of the TNBP showed that a katabatic event occurred during the three-day period between the two CTD casts (Fig. 2b). This extraordinary water-column mixing event was accompanied by intensified offshore sea ice export, as indicated by the sea ice plume in the satellite image taken on May 8 (Fig. 1b).

Fig. 3. CTD casts of (a) potential temperature, (b) salinity, and (c) potential density in the Terra Nova Bay Polynya during the PIPERS cruise on May 6 and 9, 2017. The locations of the CTD casts are labeled with circles in Fig. 1a-b. (d) Profiles of potential density sampled at the location labeled by the purple circle in the idealized Run B4 (Fig. 6a) on Day 0 and 6.

In order to highlight the influence of an ice tongue and a headland, satellite images of the TNBP during katabatic events in February and March 2015 are shown in Fig. 1c-h. During this period, sea ice started to accumulate in the TNBP. As the katabatic winds pushed new frazil and pancake ice northeastward away from the polynya, an offshore ice plume and an anticyclonic (counterclockwise) vortex to the north of the TNBP were formed. At the end of February, an iceberg detached from the Nansen Ice Shelf started to move offshore at a speed of ~0.3 m s^{-1} (Fig. 1c-d). It later entered the vortex and kept on moving counterclockwise in the vortex for more than three weeks. The spinning motion of the iceberg in the vortex remained pronounced even during later times when the sea ice cover became thicker (Fig. 1g-h), indicating that the vortex flow pattern still existed under the sea ice cover.
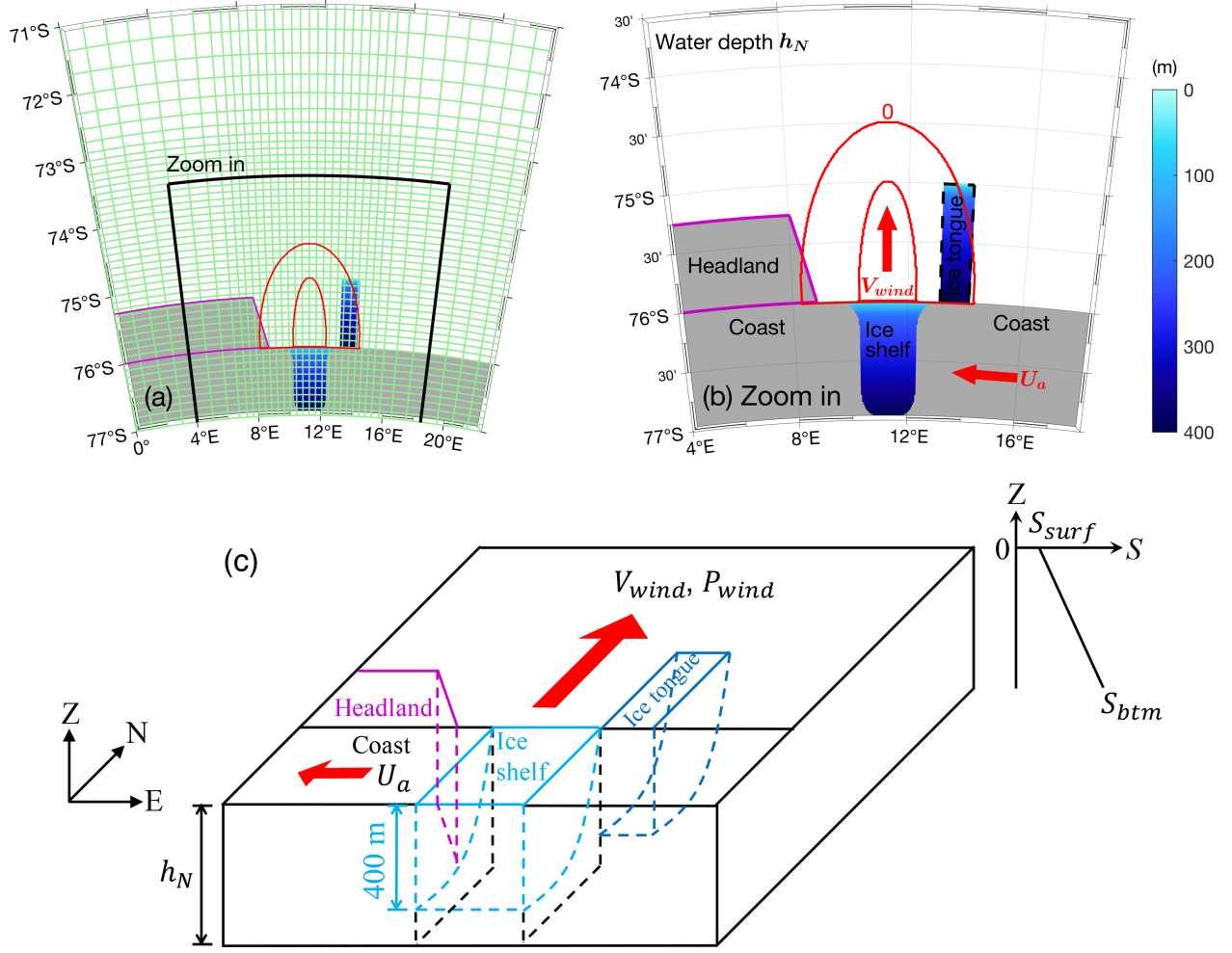
Close examination of the satellite MODIS images shows that this surface pattern of the TNBP circulation occurred in the early winters of all data-available years, 2000–2022 (not shown). Meanwhile, wintertime (April–September) winds in the region (Fig. 2a) were strong, frequently

153   falling into the katabatic regime ($\geqslant 25$ m s^{-1}; Rusciano et al. 2013). Analysis of the wind data in

154   2017 shows that winds at the TNBP oscillated strongly within the frequency band of 2–5 days (Fig.

155   2c) and that the dominant wind direction was offshore toward the east (Fig. 2d). Such strong

156   offshore winds can presumably sustain the offshore ocean current in the polynya region and the

157   anticyclonic vortex to the immediate north of the polynya, despite the sea ice cover. These ocean

158   circulation patterns likely affect the distribution of newly formed PSW and vertical mixing in the

159   water column of the TNBP.

160   This study provides a mechanistic understanding of how an ice tongue and a headland

161   could jointly influence water-column destratification in a polynya. Due to complexity in the

162   associated three-dimensional flow, it is difficult to incorporate the influence of an ice tongue or a

163   headland in a quantitative scaling analysis. Instead, this Part II study focuses on providing a

164   qualitative description of the first-order influence of an ice tongue and a headland. We hypothesize

165   that they affect the wintertime destratification process by altering the polynya circulation and then

166   the PSW dispersal in a polynya. The TNBP is used as an example to guide the model design. But

167   the result should be applicable to other coastal polynyas with similar morphological settings.

168

169   **2. Model Setup**

170   The coastal polynya model used in this study is based on the MIT General Circulation

171   Model (MITgcm; Marshall et al. 1997) and the details of the modules used in this study are

172   described in Part I. The model has an idealized configuration that spans 22.5° in longitude and 6°

173   in latitude. It includes a flat bottom of 500 m deep and an ice shelf with a cavity underneath that

174   incises into the continent to the south (Fig. 4). An idealized polynya is formed by an offshore wind

175   blowing from the ice shelf into the ocean. The horizontal grid spacing in the central study area

176   around the polynya is ~1 km, increasing northward toward the open boundaries. The vertical grid

177   is uniform with a layer thickness of 10 m. To track the PSW, passive tracer concentration is

178   constantly restored to 1 at the polynya surface where sea ice concentration is below 70%.

179

Fig. 4. (a) An aerial view of the model domain and grid and (b) a zoomed-in view of the region marked by black lines in (a). Green lines in (a) depict every 10 horizontal grid cells; the grey regions in (a) and (b) indicate land; the filled color shows the vertical position of the interface between the ice shelf/tongue and ocean, i.e., thickness of the ice shelf/tongue; red ellipses outline regions of the offshore katabatic wind V_{wind} and its inner region of maximum speed; red arrows in (b) indicate the directions of V_{wind} and the alongshore easterly winds, U_a, in Run B2, B5 and B6; purple lines in both (a) and (b) denote the shape of the headland; the black dashed line in (b) outlines the lateral boundaries of the ice tongue; (c) a three-dimensional schematic illustration of the model setup and the initial salinity profile.

In this Part II study, an ice tongue and a headland are added to the model, while other aspects of the model remain the same as in Part I. The idealized ice tongue is located to the immediate east of the ice shelf opening and the polynya, and has a 3-dimensional shape qualitatively similar to the Drygalski Ice Tongue next to the TNBP (Stevens et al. 2017). In particular, the ice tongue is 111 km long (1 degree in latitude) in the cross-shore direction and 28 km wide in the alongshore direction. Its draft gradually reduces from 400 m on the coast to 0 at its

196 offshore end. In some of the simulations, a headland is placed west of the ice shelf opening,
197 extending over the whole water column (Fig. 4). This model configuration represents the general
198 setting around some of the Antarctic coastal polynyas, e.g., the TNBP and the Mertz Polynya,
199 including the relative position of the coastline, ice shelf, ice tongue and katabatic winds. It does
200 not include any small-scale icescape and coastline geometry, or reproduce the orientation of any
201 specific polynya. It also neglects complex seafloor topography. Because this study focuses on
202 capturing the canonical circulation in a representative Antarctic coastal polynya and analyzing the
203 first-order dynamics of an ice tongue and a headland affecting polynya *local* destratification,
204 influences of smaller-scale coastline geometry, ice shelf/tongue morphology, polynya orientation,
205 and seafloor topography are neglected here. Their influence on the polynya circulation and
206 stratification is left for future studies. Note that the directions described in this study refer to those
207 in the model setup and do not necessarily apply to specific polynyas in the ocean. Other factors of
208 the model, such as initial stratification, offshore winds, and alongshore winds, are kept the same
209 as the base runs in Part I. This consistency in the model setup allows for a direct comparison of
210 the model results to examine the influences of the ice tongue and headland. This choice is also
211 supported by the fact that katabatic winds at some Antarctic coastal polynyas show similar
212 characteristics (e.g., speed and fluctuation frequencies), as indicated by winds observed at the
213 TNBP (Fig. 2) and the Vincennes Bay Polynya (Fig. 2 in Part I).

214   A total of 6 base model runs, B1-6, are analyzed in this study. Run B1 and B2 have been
215 examined in Part I. B3-6 are modified from B1 with the addition of an ice tongue, a headland and
216 alongshore easterly wind with the speed of U_a (Table 1). B3 is the same as B1, except for the
217 addition of an ice tongue of 111 km long. To consider the influence of the ice tongue length, a set
218 of 9 runs, B3-IT, with different ice tongue length (11–100 km) are performed. Other factors in B3-
219 IT are the same as in B3. B4 includes both an ice tongue and a headland, and is qualitatively similar
220 to the setting of the TNBP. Results of the B4 simulation will be qualitatively compared to
221 observations in the TNBP during wintertime katabatic events. B5 and B6 are the same as B3 and
222 B4, respectively, except with the addition of alongshore easterly winds. Their comparisons will
223 reveal how alongshore winds interact with complex coastal geometry and modify the polynya
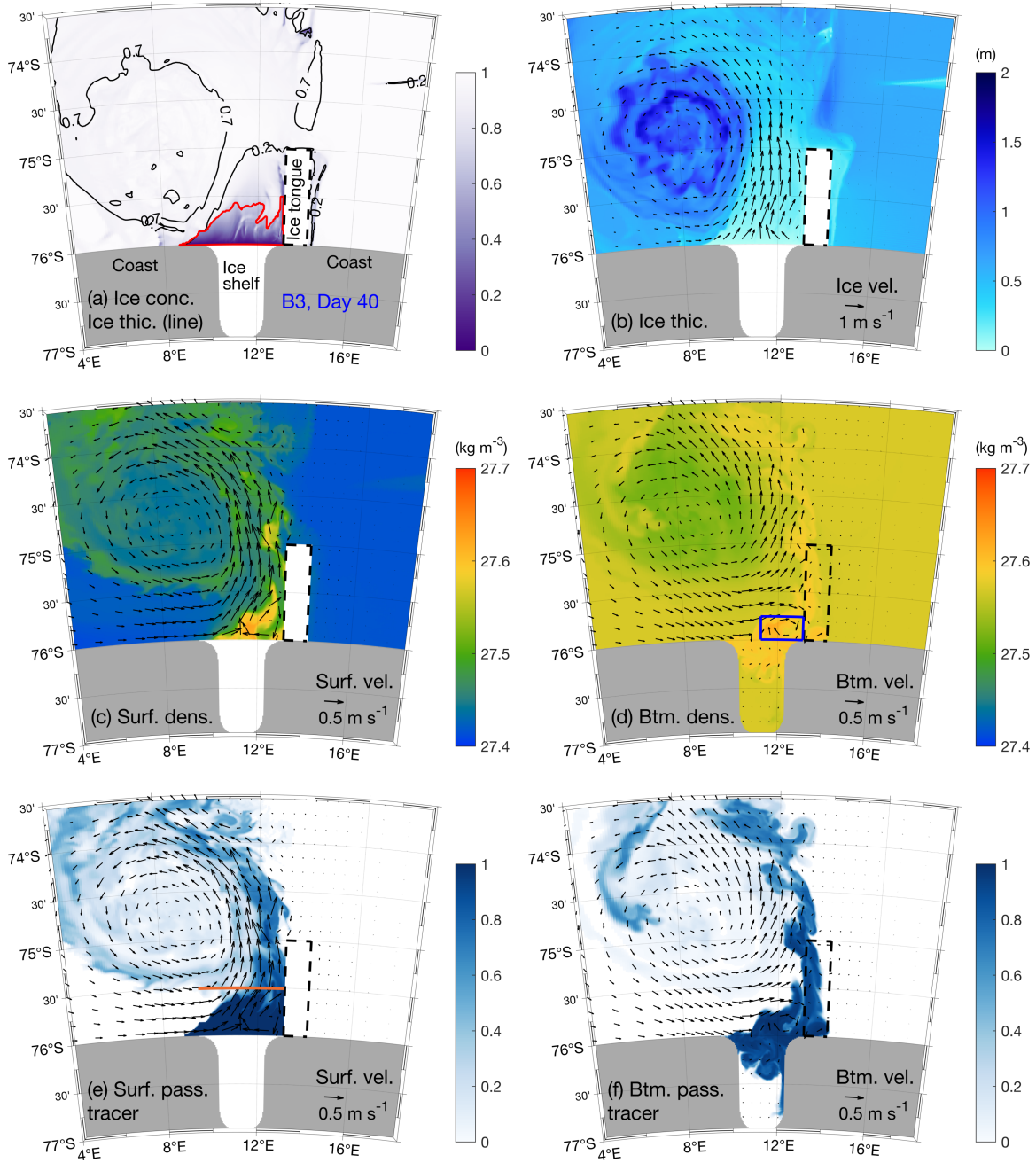224 destratification process.

225

Run labels	U_a (m s^{-1})	Ice tongue length	Headland
B1	0	0	No
B2	10	0	No
B3	0	Full length: 111 km	No
B3-IT	0	11–100 km	No
B4	0	Full length: 111 km	Yes
B5	10	Full length: 111 km	No
B6	10	Full length: 111 km	Yes

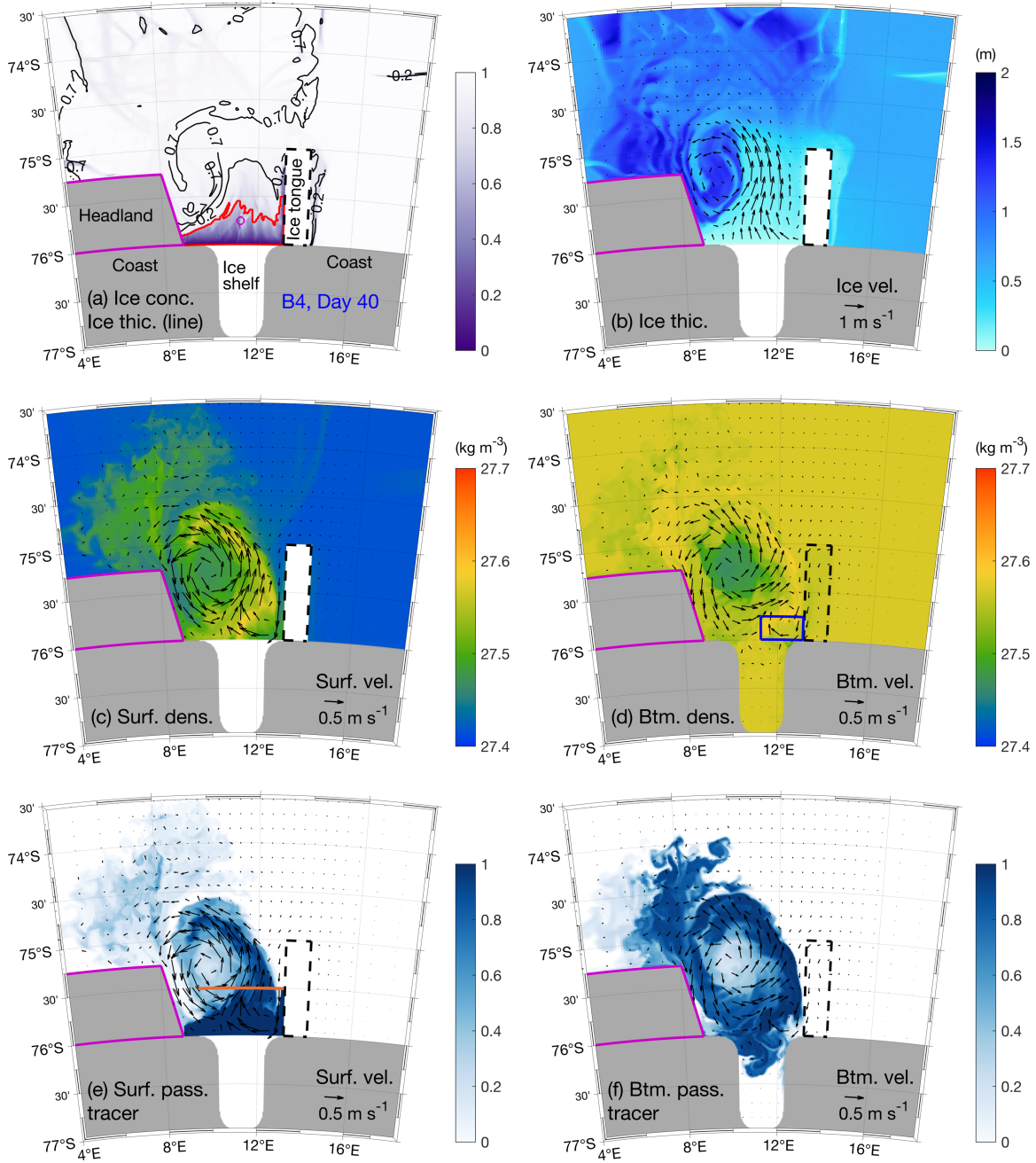226   **Table 1.** Base runs and their difference from B1.

227

3. Results

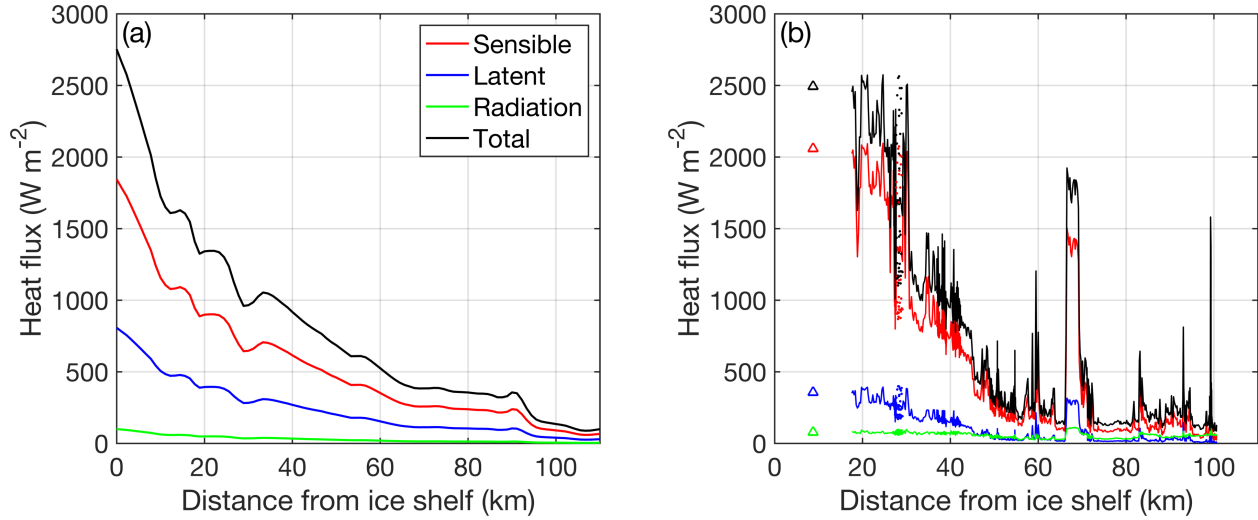*a. General Pattern of Modeled Polynyas*

230   Snapshots of sea ice concentration and thickness, potential density, and passive tracer
231 concentration on model Day 40 (Figs. 5 and 6) show that a coastal polynya is formed at the center
232 of the wind field at the ice shelf front in both Run B3 and B4. Meanwhile, their sea ice and ocean
233 fields differ drastically and also deviate significantly from the patterns in B1 (Fig. 5 in Part I). To
234 validate the model, we qualitatively compare modeled fields in B4 on Day 40 (representative of
235 the early winter condition) with observed sea ice and ocean conditions. Run B4 is chosen here
236 because its configuration qualitatively resembles the TNBP.

237

Fig. 5. Snapshots of model fields on Day 40 from Run B3: (a) sea ice concentration (color) and thickness (black contours in meters); (b) sea ice thickness (color) and sea ice velocity (arrows); potential density (color) and velocity (arrows) at the (c) surface and (d) bottom; concentration of passive tracer (color) originating from the polynya surface and velocity (arrows) at the (e) surface and (f) bottom. The red line in (a) outlines the coastal polynya on Day 40; the orange line in (e) indicates the transect where offshore fluxes are integrated vertically and zonally and shown in Fig. 16; the blue box in (d) indicate the ice tongue end corner region where the surface and bottom densities are averaged and shown in Fig. 11.

Fig. 6. Snapshots of model fields on Day 40 from Run B4: (a) sea ice concentration (color) and thickness (black contours in meters); (b) sea ice thickness (color) and sea ice velocity (arrows); potential density (color) and velocity (arrows) at the (c) surface and (d) bottom; concentration of passive tracer (color) originating from the polynya surface and velocity (arrows) at the (e) surface and (f) bottom. The red line in (a) outlines the coastal polynya on Day 40; the purple circle in (a) denotes the location of potential density plotted in Fig. 3d; the orange line in (e) indicates the transect where fluxes are integrated vertically and zonally and shown in Fig. 16; the blue box in (d) indicate the ice tongue end corner region where the surface and bottom densities are averaged and shown in Fig. 11.

257

Fig. 7. (a) Snapshots of modeled surface heat fluxes out of the ocean along the cross-shore centerline of the ice shelf in Run B4 on Day 40, as a function of the distance from the ice shelf. Positive values indicate heat loss from the ocean. (b) surface heat fluxes measured in the Terra Nova Bay Polynya on May 8, 2017 (Guest 2021).

Because the polynya system is largely forced by winds, applying representative atmospheric conditions and reliable air-sea interaction parameterization is important for the success of the model simulations. Thus, we here provide a qualitative model validation by comparing modeled surface heat fluxes with those observed in the TNBP during the PIPERS expedition in May 2017 (Guest 2021), even though the atmospheric and ocean conditions in the idealized model do not exactly match the condition during the observation. The comparison (Fig. 7) shows that the model captures general trends of the observed heat fluxes along the centerline of the polynya, including the overall magnitude of the fluxes, their relative contributions, and their cross-polynya distributions. In particular, both the model and observations show the dominance of sensible heat flux, followed by latent flux and radiation flux. All fluxes have the highest magnitude in the ice shelf front region where the total heat flux reaches about 2500 W m^{-2}, and they all decrease gradually offshore. The highest fluxes occur in the ice shelf front region because the katabatic winds are the strongest and the sea ice concentration is the lowest there, both of which enhance the heat exchange between the air and ocean. Further offshore, the katabatic wind speed remains high, but sea ice concentration and thickness increase due to freezing and compression, and sea ice hinders the air-sea heat exchange. Note that, small-scale variabilities in the observed fluxes are presumably caused by ice floes or leads (Guest 2021), which are not resolved by the

14

280 model. The general agreement between the modeled and observed heat fluxes confirms that the
281 prescribed surface forcings and the air-sea interaction parameterization in the model reasonably
282 capture key features of the polynya forcings.

283   The model produces an offshore-flowing plume and a vortex pattern in the sea ice fields
284 (Fig. 6b), similar to those shown in the satellite images (Fig. 1c-h). This indicates that the model
285 qualitatively captures the wind-driven sea ice and ocean flows on the surface. Below the surface,
286 the model captures the deepening of the surface mixed layer within a few days of a katabatic wind
287 event (Fig. 3d). In particular, water density in the initially stratified top 300 m is homogenized on
288 Day 6. This pattern also qualitatively resembles the deepening of the surface mixing layer on May
289 6–9, 2017. These demonstrate the model's capability in capturing key sea ice and ocean dynamics
290 in Antarctic coastal polynyas as represented by the TNBP, allowing us to diagnose the underlying
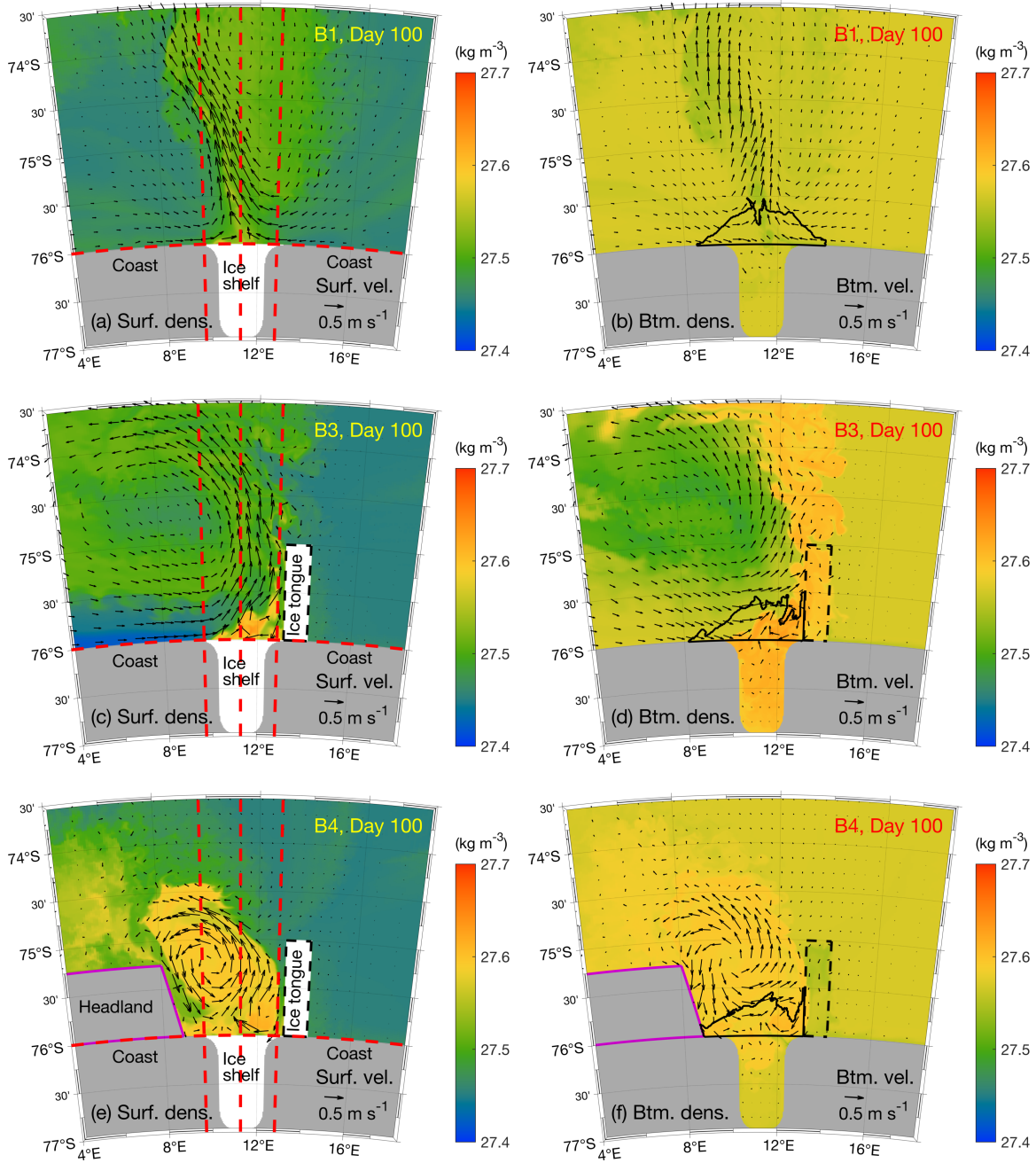291 dynamics of polynya circulation from the simulations.

292   In B1, in the absence of an ice tongue and a headland, a sea ice and PSW plume driven by
293 the katabatic winds flows northward offshore in the polynya region (Fig. 5 in Part I). The plume
294 gradually turns to its left under the influence of the Coriolis force. To compensate for the plume
295 offshore transport, an eastward (westward) current toward the polynya is formed on the coast to
296 the west (east) of the polynya. To the far west and east of the plume, the flow is weakly southward,
297 which, together with the coastal currents and the plume outflow, forms a weak anticyclonic
298 (cyclonic) flow pattern with a radius of 100–150 km to the west (east) of the plume. Together, they
299 form a dipole flow pattern that persists deep into the water column.

300   In B3, with the addition of an ice tongue, the relatively symmetric flow patterns in the
301 alongshore direction breaks down, and the ice tongue blocks sea ice and ocean circulation to the
302 east side of the polynya (Fig. 5b-d). Yet on the west side, the wind stress shear induces an
303 anticyclonic vortex in sea ice and ocean fields. The plume outflow can be considered as the eastern
304 edge of the vortex. Compared to the anticyclonic flow pattern in B1, the anticyclonic vortex in B3
305 is stronger and shifted slightly to the east. The maximum surface and bottom flow speeds in the
306 anticyclonic vortex in B3 are ~0.5 m s^{-1} and ~0.3 m s^{-1}, respectively. Examination of the temporal
307 evolution of the model field reveals that sea ice is gradually entrained into the vortex and converges
308 toward the vortex center forming thicker ice there (Fig. 5b). Meanwhile, some PSW is transported
309 offshore away from the polynya throughout the water column (Fig. 5e-f). On Day 40, high-density

310   water appears on the bottom at the corner of the ice tongue and ice shelf (blue box in Fig. 5d;

311   hereafter referred to as *ice tongue end corner*) and within the ice shelf cavity (Fig. 5f), indicating

312   that the PSW has already penetrated through the entire water column reaching the bottom.

313   Therefore, the water column of part of the polynya region has been completely mixed on Day 40.

314   This is much faster than the case without the ice tongue (B1), where it takes the PSW more than

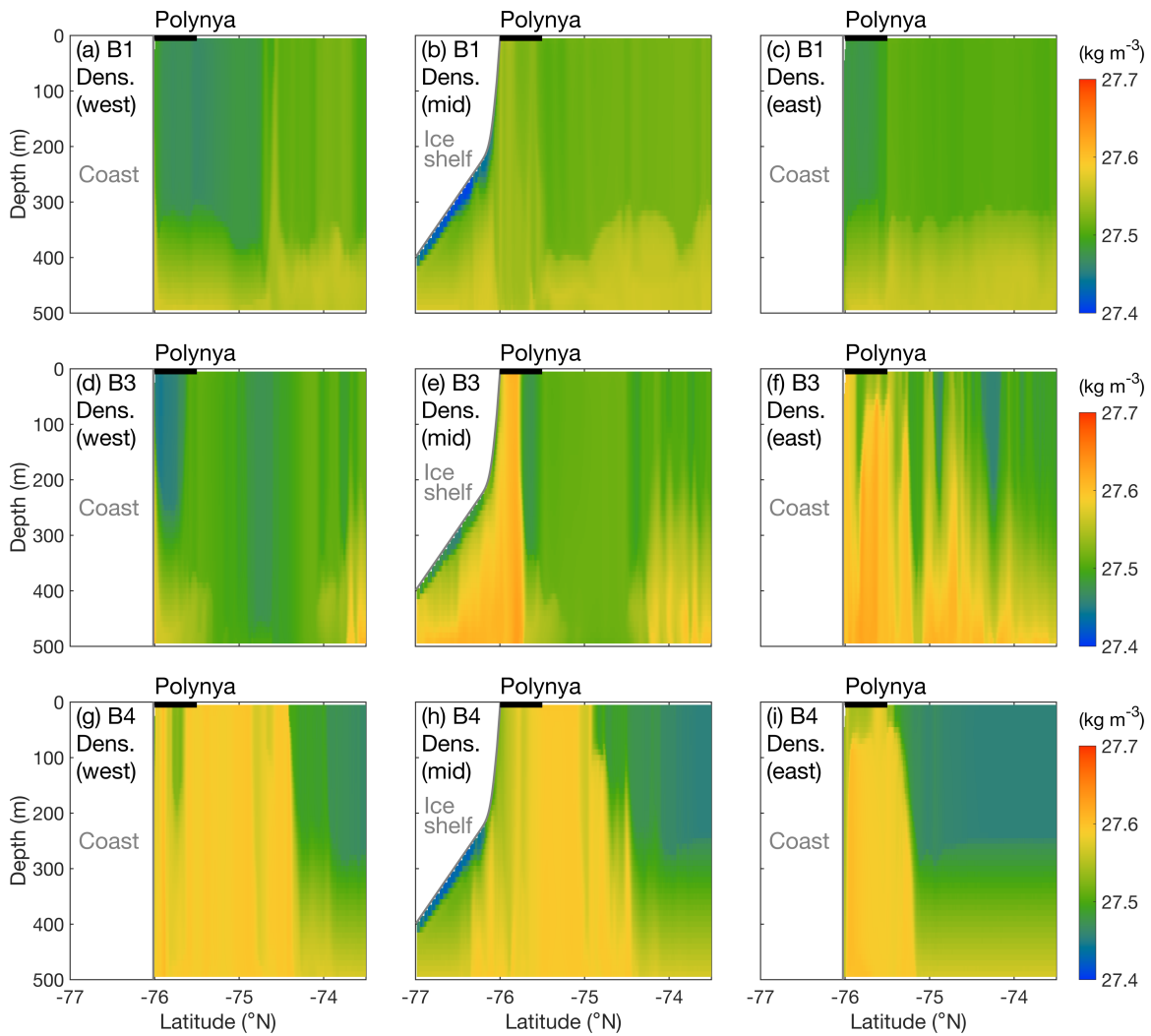315   100 days to reach the bottom.

316   In B4, with an ice tongue and a headland, the patterns of sea ice distribution and ocean

317   circulation on Day 40 differ from those in B1 and B3. Specifically, the headland to the west of the

318   polynya suppresses the lateral compensating flow from the west, while the ice tongue to the east

319   of the polynya blocks the sea ice and ocean flows on the east side. A compact anticyclonic vortex

320   is formed to the northwest of the polynya with a radius of ~50 km, smaller than the vortex formed

321   in B3 without the headland. The maximum surface and bottom flow speeds in the vortex in B4 are

322   ~1 m s^{-1} and ~0.5 m s^{-1}, respectively, higher than those in B1 and B3. The shrinking of the vortex

323   and strengthening of the vortex flow in B4 is caused by the headland. The dynamics of the vortex

324   formation will be discussed in Section 3b. Part of the PSW is entrained into the vortex, and a

325   portion of that PSW re-enters the polynya region through the eastward compensating flow to the

326   west of the polynya. While the PSW concentration remains low at the center of the vortex on Day

327   40 (Fig. 6e-f), the bottom density at the vortex center is similar to that at the surface (Fig. 6c-d),

328   lower than the surrounding region. This indicates that the low-density low-salinity surface water

329   has been subducted at the vortex center. Relative to B3, B4 shows lower bottom density at the ice

330   tongue end corner on Day 40, suggesting slower PSW sinking and polynya water-column

331   destratification.

332

Fig. 8. Snapshots of potential density (color) and velocity (arrows) at the surface (left) and bottom (right) on Day 100 from Runs B1 (a-b), B3 (c-d), and B4 (e-f). Black lines in (b), (d), and (f) outline the surface area of the coastal polynya on Day 100. The red dashed lines represent three cross-shelf transects in the west end, middle, and east end of the polynya, and the along-coast transects near the ice shelf front.

339   Both B3 and B4 show a much faster destratification in the polynya region than B1. This

340 difference is more pronounced later in the simulations, such as on Day 100 (Fig. 8), when both

341 surface and bottom density fields differ greatly among these three runs. While the PSW has barely

342 reached the polynya bottom in B1 on Day 100, in B3, a substantial amount of PSW has sunk to

343 the bottom and occupied the ice shelf cavity. The bottom density in B4 is higher than that B1, but

344 lower than in B3. Volume integrations of the modeled PSW passive tracer show that the amount

345 of PSW residing in the ice shelf cavity on Day 100 reduces from B3 to B4 by 27%.
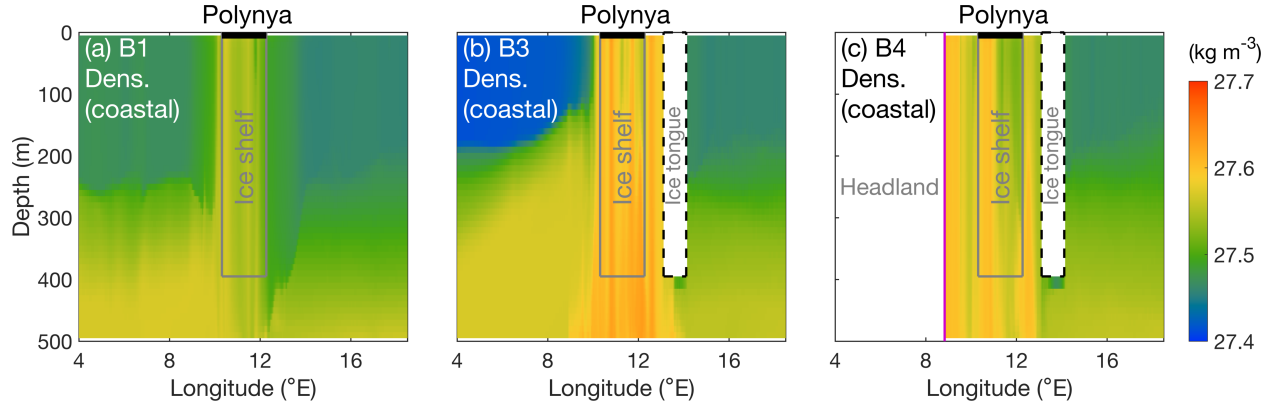
346

348   **Fig. 9.** Cross-sections of potential density on Day 100 along the three red dashed cross-shore lines in
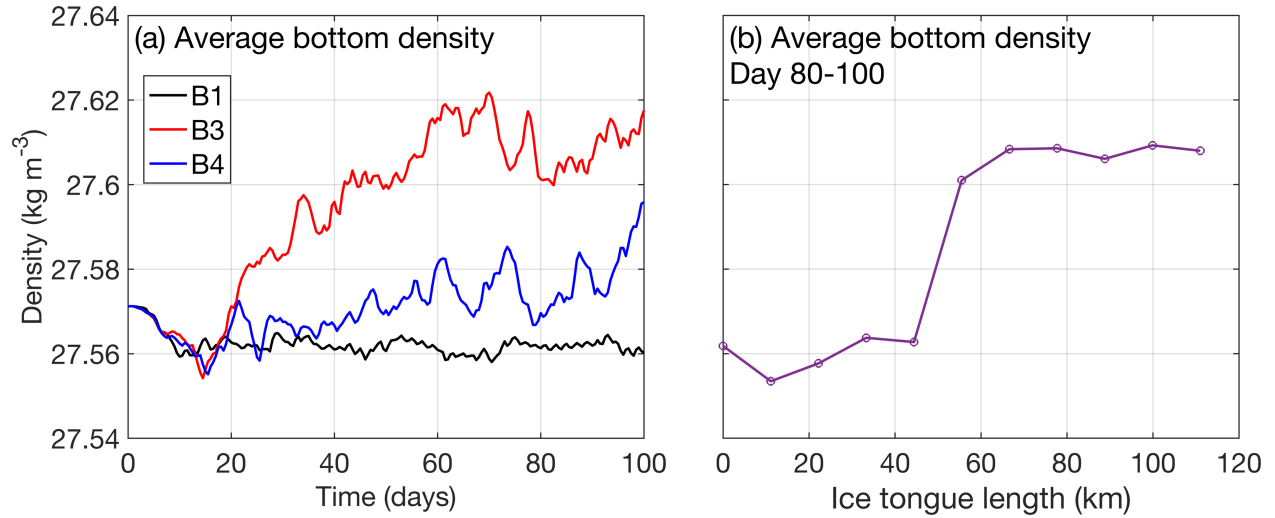349 (a-c) Fig. 8a for Run B1, (d-f) Fig. 8c for Run B3, and (g-i) Fig. 8e for Run B4.

350

18

351   Another difference among B1, B3, and B4 is the PSW circulation in the polynya water
352   column. In B1, PSW mainly moves directly offshore of the polynya. In contrast, PSW stays near
353   the ice tongue end corner in B3, while it spreads out in the polynya region in B4. This is illustrated
354   in the cross-shore transects at the polynya's west end, middle, and east end (Fig. 9) and the
355   alongshore transect near the coast (Fig. 10). In B1 on Day 100, much of the PSW is diffusively
356   distributed in the water column north of the polynya (Fig. 9b); in B3, more PSW appears in the
357   water column below the polynya on the middle and eastern cross-shore transects close to the ice
358   tongue (Fig. 9d-f); in B4, the PSW is more uniformly distributed on the three cross-shore transects
359   (Fig. 9g-i). The middle transects also show more PSW intruding into the ice shelf cavity in B3
360   than in B4 and B1 (Fig. 9b, 9e, and 9h); the eastern transects show more offshore fresher (less-
361   dense) water intruding onshore toward the polynya in B4 than that in B3 (Fig. 9f and 9i). The
362   along-coast transects near the ice shelf front show more PSW sinking to the bottom over the entire
363   ice shelf front in B3 than B4 and B1 (Fig. 10), consistent with the higher density of polynya bottom
364   water in B3 than B4 and B1 on both Day 40 (Fig. 5d vs. 6d; B1 not shown) and Day 100 (Fig. 8b
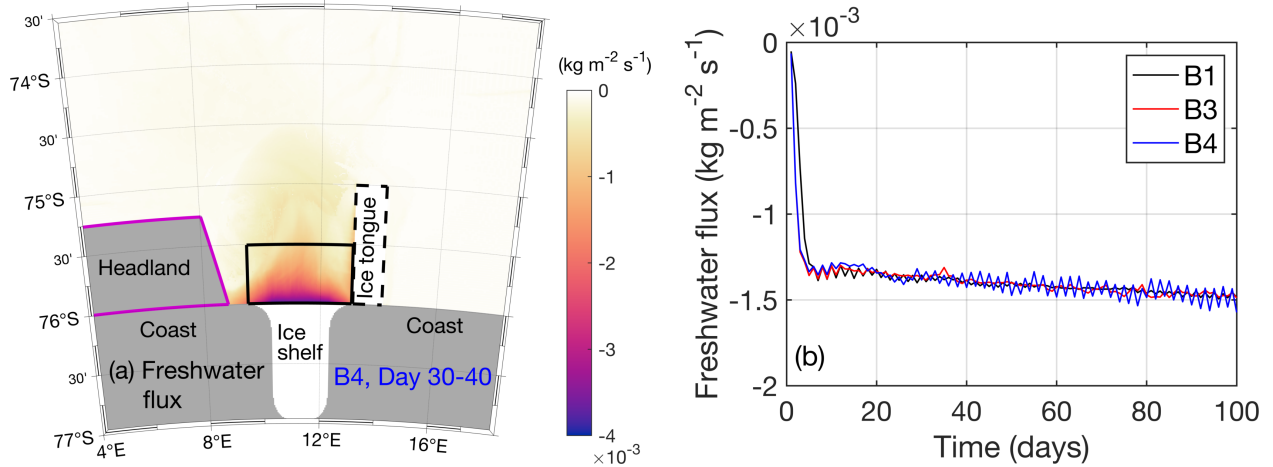365   vs. 8d and 8f).

366   To examine the representativeness of this bottom density comparison over the simulation
367   period, we compare the time evolution of polynya bottom density averaged in the box at the ice
368   tongue end corner in the first 100 days in B1, B3, and B4 (Fig. 11a). After the initial adjustment,
369   the bottom density in B3 is persistently the highest, B4 has an intermediate bottom density, and
370   B1 has the lowest bottom density. This confirms that B3 has the highest polynya destratification
371   rate, followed by B4 and then B1.

372

Fig. 10. Cross-sections of potential density on Day 100 along the red dashed along-coast lines in (a) Fig. 8a for Run B1, (b) Fig. 8c for Run B3, and (c) Fig. 8e for Run B4.

Fig. 11. (a) Time evolution of the averaged bottom density at the ice tongue end corner (the blue box in Fig. 5d and 6d) in Runs B1, B3, and B4; (b) Mean bottom densities at the ice-tongue-polynya corner in Day 80-100 in Runs B3-IT with different ice tongue length.

Fig. 12. (a) Net surface freshwater flux into the ocean averaged over Day 30-40 in Run B4; (b) time evolution of the net surface freshwater flux averaged within the black box outlined in (a) in Runs B1, B3, and B4. Note that negative freshwater flux means increasing salinity in the ocean.
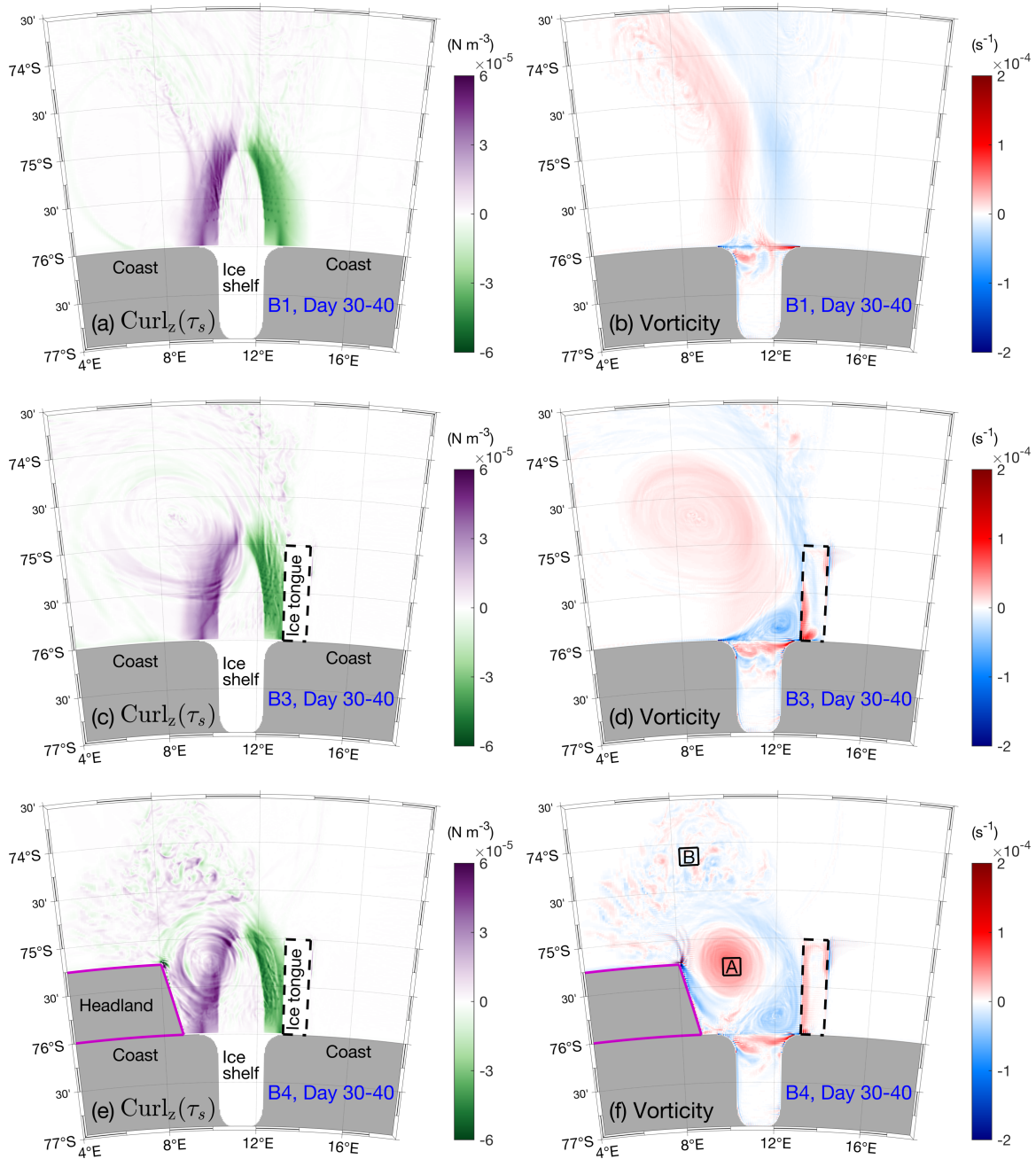
b. Dynamics of PSW Circulation

Here we investigate the mechanism behind the differences in the modeled polynya destratification rates. First, we compare the surface buoyancy fluxes in the simulations to examine whether the differences result from variations in the PSW source. Both B1 and B3 have a similar pattern of surface freshwater flux into the ocean as in B4 (Fig. 12a). Time evolution of the averaged freshwater flux in the polynya region is similar in B1, B3, and B4 (Fig. 12b), despite small-amplitude oscillations in B4 caused by oscillations of the vortex (see Section 3c). This similarity is not surprising as the atmospheric forcings in these simulations are the same and the polynya areas are very similar. Therefore, adding the ice tongue or the headland does not change the surface buoyancy flux in the polynya region, and differences in the PSW flows in the simulations are likely caused by variations in the modeled polynya circulations.

As shown in the Part I paper, polynya circulation is largely driven by winds. Runs B1, B3 and B4 are forced by the same winds and have the same pattern of surface stress curl with a positive (negative) curl on the western (eastern) edge of the wind forcing region (Fig. 13). The circulation differences among B1, B3, and B4 are thus caused by different modulation of the ocean response to the wind forcing. In B1, with no ice tongue or headland, positive and negative relative vorticity appears on the west and east sides of the polynya outflow, respectively (Fig. 13b), corresponding to the aforementioned anticyclonic and cyclonic flow pattern (Fig. 5 in Part I). This dipole flow

21

405   pattern could be attributed to convergence and divergence of the surface Ekman transport to the
406   west and east of the wind forcing region, respectively. Close examinations of the model results
407   show that they drive sea level set-up and set-down on the west and east sides of the offshore plume,
408   respectively (not shown), which, through geostrophic balance, drives the anticyclonic and cyclonic
409   flows. The vorticity of these flows originates from the positive and negative wind stress curl in the
410   wind forcing region (Fig. 13a). From the perspective of vorticity balance, as shown below with B4
411   as an example, the wind-driven plume outflow transports the positive and negative vorticity
412   generated in the polynya region by the wind stress curl offshore. Once leaving the forcing region,
413   the flow loses the vorticity injection from the wind and starts to respond to the vorticity. That is,
414   the positive (negative) vorticity to the west (east) of the polynya starts to rotate the flow
415   counterclockwise (clockwise) and form the large dipole flow pattern, which includes the eastward
416   (westward) coastal compensating flow to the west (east) of the polynya (Fig. 8a-b). Model
417   diagnostics (not shown) indicate that the momentum of the eastward and westward coastal flows
418   is in a rough balance, which keeps the polynya outflow along the centerline of the ice shelf before
419   the Coriolis force pushes the outflow to the west.

420   In B3, the ice tongue blocks the flow and clockwise rotation on the east side of the polynya,
421   and only the positive relative vorticity to the west of the polynya can rotate the velocity and form
422   the anticyclonic vortex (Fig. 13d). This causes an asymmetrical flow pattern across the polynya
423   outflow. As a result, the eastward coastal return flow to the west of the polynya is the only flow
424   compensating for the polynya outflow and thus greatly strengthened compared to that in B1 (Fig.
425   8a-d). This strong coastal flow pushes the polynya outflow eastward against the ice tongue. There
426   is no room for any return flow to develop to the east of the polynya outflow. The counterclockwise
427   turning of the flow in the anticyclonic vortex from the eastward coastal current to the offshore
428   outflow creates a wedge at the ice tongue end corner with a negative relative vorticity. The cyclonic
429   flow inside the wedge is separated from the polynya outflow, which traps and then accumulates
430   some of the PSW. Because this part of the PSW is not carried offshore by the offshore plume, it
431   sinks quickly and breaks down the water-column stratification in the corner efficiently. This differs
432   from B1, where the polynya circulation is more symmetric with coastal compensating flows from
433   both the west and east meeting in the middle of the ice shelf front, which causes more PSW to be
434   transported away from the polynya region by the outflow and thus suppresses local sinking of the
435   PSW.

436

Fig. 13. (left) Curl of the ocean surface stresses and (right) water-column-averaged relative vorticity averaged over Day 30–40 in Runs B1 (a-b), B3 (c-d) and B4 (e-f). The black boxes in (f) indicate the regions A and B where the terms in the vorticity equation are averaged and plotted in Fig. 15.

441

442   The blocking effect of the ice tongue changes with the ice tongue length. Runs B3-IT with
443   ice tongues of different lengths show a dramatic increase of the bottom density at the ice tongue
444   end corner on Day 80–100 when the ice tongue length increases from 45 km to 55 km (Fig. 11b).
445   The modeled bottom density changes very little when the ice tongue is shorter than 45 km or longer
446   than 55 km. The ice tongue length at which the transition occurs coincides with the cross-shore
447   width of the polynya, ~45 km (Fig. 8d). Close examination of the B3-IT simulations shows that,
448   when the ice tongue is shorter than the polynya width (Fig. 14a-b), the flow to the east of the
449   polynya outflow is not effectively blocked, and a westward current forms at the northern end of
450   the ice tongue, which pushes the polynya outflow slightly westward away from the ice tongue.
451   This allows a southward current to develop in the space between the ice tongue and the polynya.
452   The southward flow transports water from the east into the polynya region and compensates for
453   part of the polynya outflow. This prevents the formation of a large stagnant wedge area in the ice
454   tongue end corner, and the local sinking of the PSW in the corner is thus suppressed. When the ice
455   tongue is longer than the polynya width (Fig. 14c-d), the water supply from the east to the polynya
456   region is almost entirely blocked, and the polynya outflow is pushed against the ice shelf as in Run
457   B3. Further extending the ice tongue does not significantly change the polynya circulation. These
458   confirm that blocking of the coastal compensating flow from the east into the polynya by the ice
459   tongue reduces offshore transport of the PSW, enhances local sinking of the PSW, and accelerates
460   destratification of the polynya water column.

461   In B4, the headland blocks the large-scale circulation to the west of the polynya and
462   restricts the region of the anticyclonic flow (Fig. 8e). It causes the anticyclonic vorticity to
463   concentrate in a small region to the immediate east of the headland (Fig. 13f), which resembles the
464   observed vortex in the TNBP (Fig. 1c-h). To understand the associated vorticity dynamics, we
465   diagnose the vorticity budget in the B4 model. Two locations (Fig. 13f), one in the anticyclonic
466   vortex under the influence of strong surface stress curl (box A) and the other in the offshore plume
467   without the influence of strong surface stress curl (box B), are selected to calculate the terms in
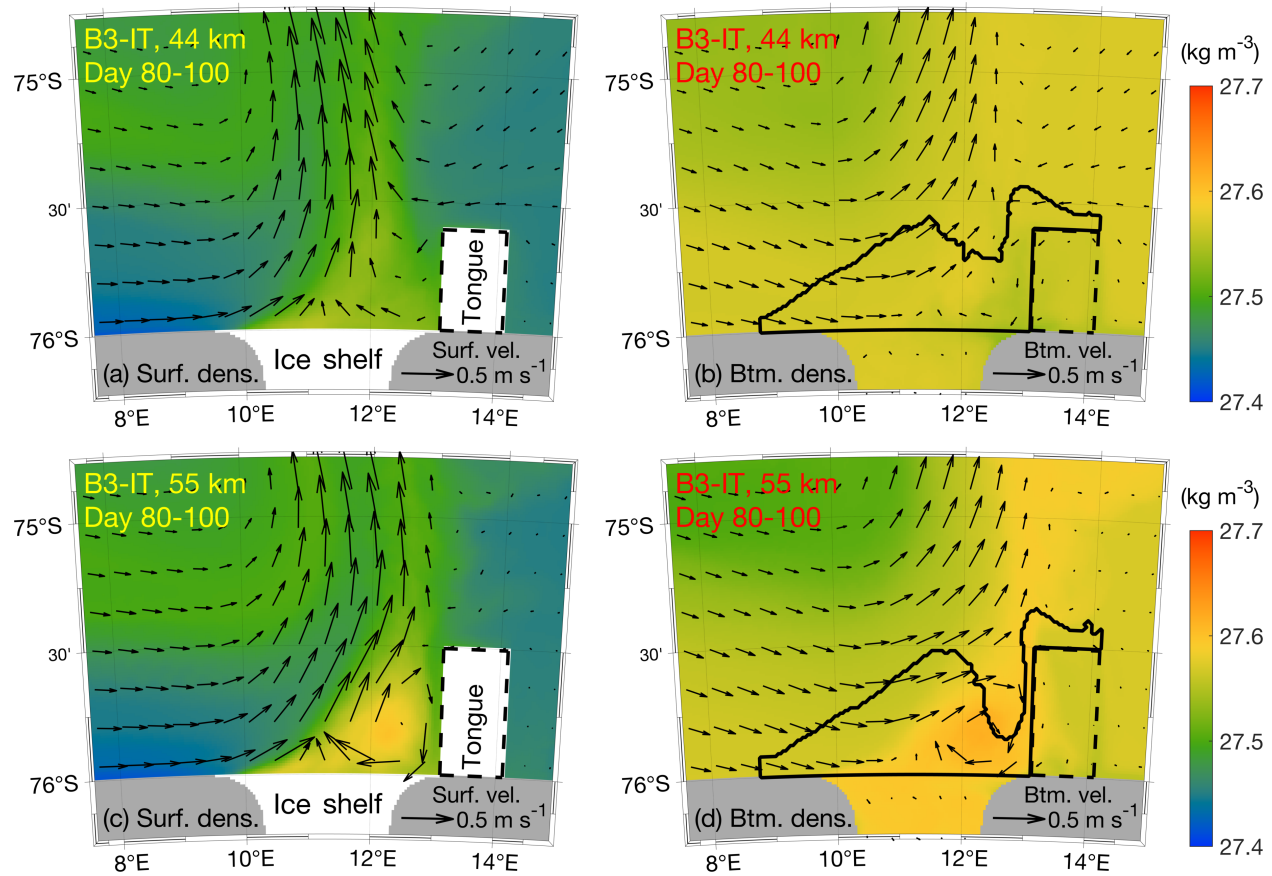468   the volume-averaged vorticity equation:

$$\frac{\partial \bar{\zeta}}{\partial t} = \overline{-(\zeta + f)\left(\frac{\partial u}{\partial x} + \frac{\partial v}{\partial y}\right)} + \overline{\left(-u\frac{\partial \zeta}{\partial x} - v\frac{\partial \zeta}{\partial y}\right)} + \overline{\frac{1}{\rho_0 h_N}\left(\frac{\partial \tau_{sy}}{\partial x} - \frac{\partial \tau_{sx}}{\partial y}\right)}$$
$$+ \overline{\frac{1}{\rho_0 h_N}\left(\frac{\partial \tau_{by}}{\partial x} - \frac{\partial \tau_{bx}}{\partial y}\right)} + \overline{\kappa_H\left(\frac{\partial^2 \zeta}{\partial x^2} + \frac{\partial^2 \zeta}{\partial y^2}\right)} \qquad (1)$$
$$+ \overline{\frac{\partial w}{\partial y}\frac{\partial u}{\partial z} - \frac{\partial w}{\partial x}\frac{\partial v}{\partial z} - w\frac{\partial \zeta}{\partial z}}.$$

469 Here, ζ is relative vorticity of the horizontal flow, f is the Coriolis parameter, u is zonal velocity,

470 v is meridional velocity, w is vertical velocity, h_N is the water depth, ρ_0 is the reference density

471 of seawater; τ_{sx} (τ_{sy}) and τ_{bx} (τ_{by}) are the surface and bottom stress in the zonal (meridional)

472 direction, respectively; κ_H is the horizontal viscosity; the overbar indicates volume-averaging. The

473 terms on the right-hand-side of (1) represent vorticity horizontal divergence, horizontal advection,

474 source from the surface stress curl, source from the bottom stress curl, horizontal diffusion, and

475 the curl of the vertical advection term in the horizontal momentum equation, respectively.

476   The vorticity diagnostics show that the dominating terms in the vorticity balance change

477 spatially. Within box A (Fig. 15a), the major vorticity balance is between the surface and bottom

478 stress curl, especially, later in the simulation when the system reaches a quasi-equilibrium state.

479 The other terms are generally secondary. This indicates that vorticity within the anticyclonic vortex

480 is mainly driven by the surface stress curl. In contrast, within the offshore box B (Fig. 15b) where

481 the surface stress is only generated by flows of the sea ice and thus weak, the main vorticity balance

482 is between the lateral advection, i.e., upstream injection, and the horizontal divergence term. The

483 net advective flux convergence of vorticity in the box is thus negligible. Detailed analysis of the

484 model results shows that horizontal divergence of the vorticity results from the small-scale

485 covariance between the vorticity and divergence of the horizontal flow, which serves as a sink of

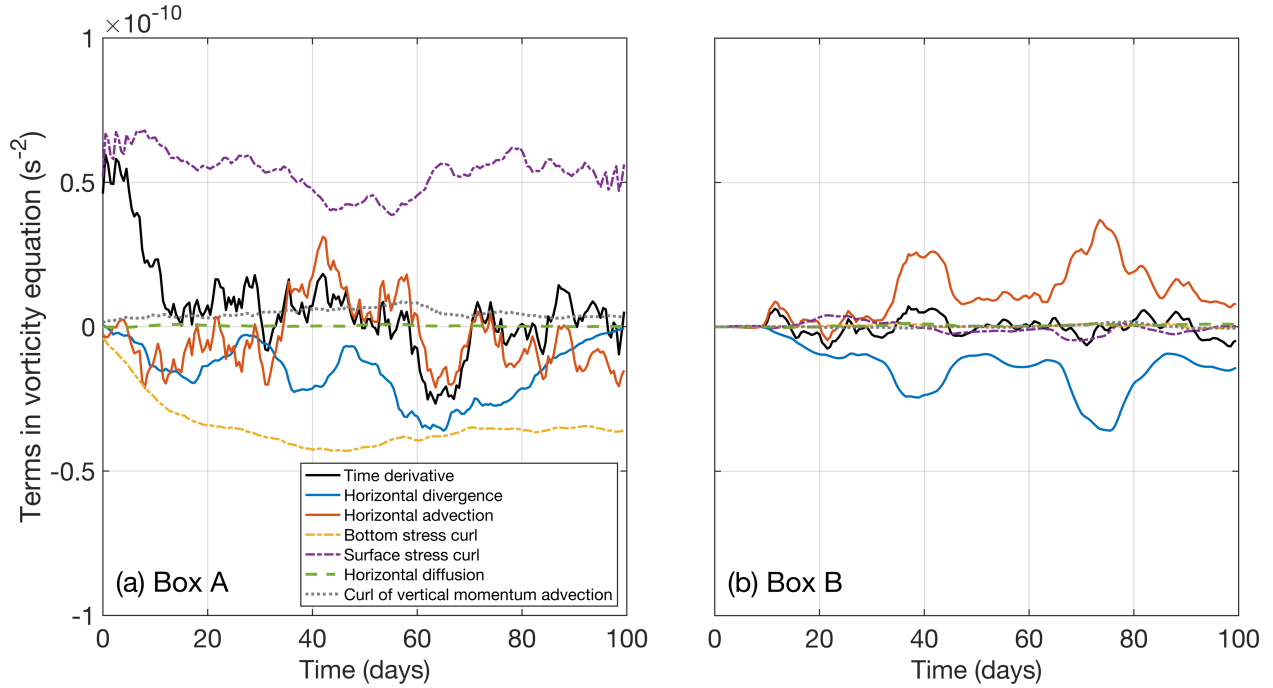486 the total relative vorticity in the system.

487   In B4, the headland also blocks the eastward coastal current. Consequently, the polynya

488 outflow is not pushed against the ice tongue as in B3, and a narrow southward current forms

489 between the ice tongue and the polynya outflow, reaching the ice tongue end corner (Fig. 8e). This

490 southward current to the east of the polynya outflow, together with the southeastward current on

491 the southwest edge of the anticyclonic vortex, volumetrically compensate for the polynya outflow.

492 Essentially, the addition of the headland to the west of the polynya causes the polynya circulation

493 in B4 to be more symmetric than that in B3. The compensating flow to the east of the polynya

494 pushes some of the PSW in the ice tongue end corner into the polynya outflow, suppresses local
495 sinking of the PSW, and slows down the destratification of the polynya water column. All these
496 suggest that coastal geometry influences polynya water-column destratification through modifying
497 polynya circulation and offshore transport of the PSW.

498

500 **Fig. 14.** Potential density (color) and velocity (arrows) at the surface (left) and bottom (right) averaged
501 over Day 80–100 in two of Runs B3-IT where ice tongue lengths are 44 km (a-b) and 55 km (c-d).
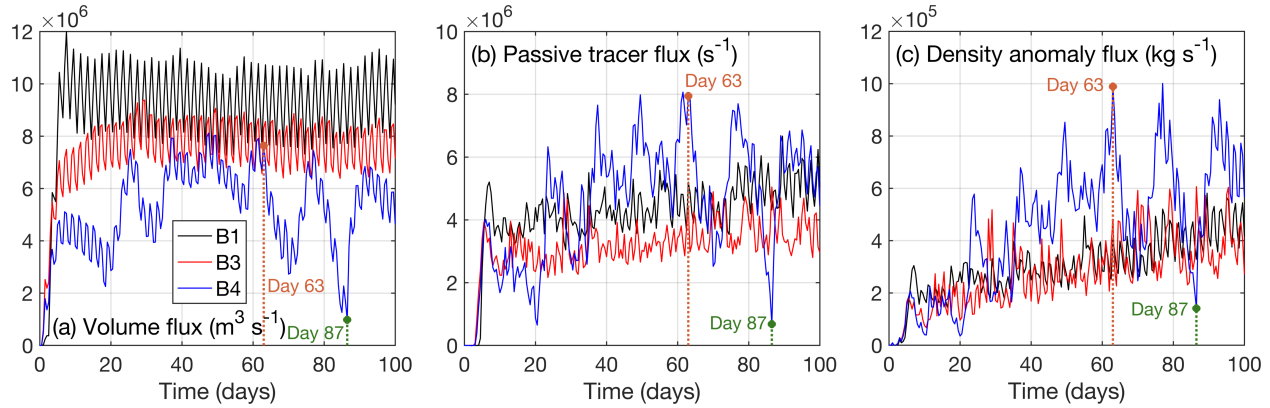502

Fig. 15. Time series of the terms in the volume-averaged vorticity equation in run B4 within (a) a nearshore box A and (b) an offshore box B, as labeled in Fig. 13f. The time series here have been smoothed with a 10-day running window.

c. Temporal Variation

To further reveal the connection among polynya circulation, offshore transport of the PSW, and polynya water-column destratification, we compare the offshore volume transport and the associated offshore loss of the PSW in Runs B1, B3, and B4. Vertically and zonally integrated fluxes of total water volume, PSW passive tracer, and density anomaly across an alongshore transect immediately offshore of the polynya (orange lines in Figs. 5e and 6e) are obtained from the simulations (Fig. 16). All fluxes exhibit oscillation with a period of 2 days, consistent with the prescribed wind fluctuation. The fluxes in B4 also exhibit strong variation on the time scale of 10–15 days. We here start with comparing temporal mean fluxes in the simulations and will analyze the strong temporal variation in B4 later in this section.

27

Fig. 16. Integrated (a) volume, (b) passive tracer, and (c) density anomaly fluxes across the transects along the orange lines in Figs. 5e and 6e for Runs B1, B3, and B4. Day 63 and Day 87 are highlighted with dotted lines.
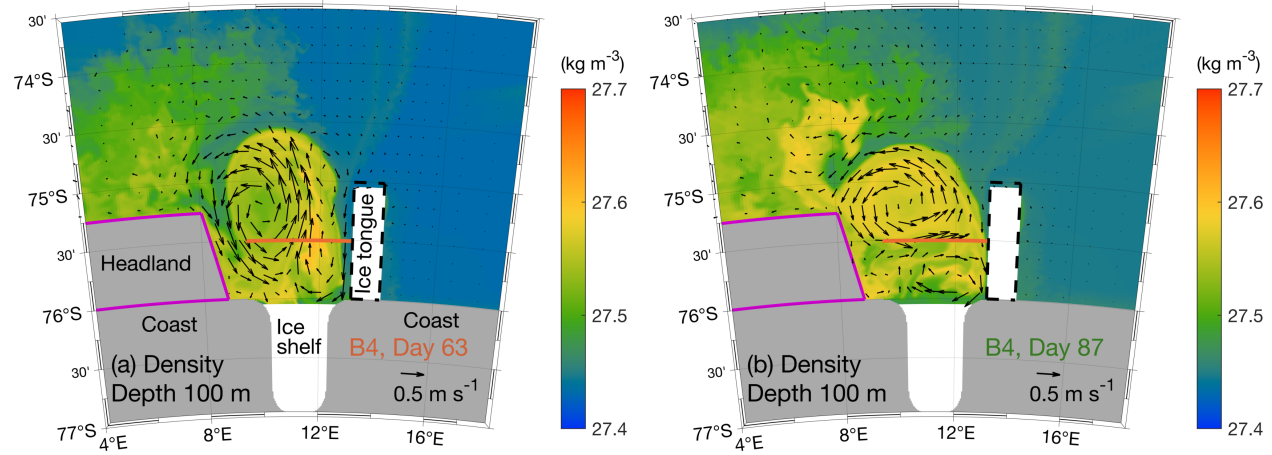
Without the ice tongue or headland (B1), the temporal mean volumetric flux of the polynya outflow is the highest. It is consistent with the water supply from the coastal currents on both sides of the polynya. The mean offshore volume flux is reduced in B3 when the ice tongue is included, which blocks the coastal compensating flow from the east. B4 has the lowest mean offshore volume flux because coastal currents on both sides are mostly blocked and replaced by weaker southward compensating flows.

The modeled PSW and density anomaly fluxes across the alongshore transect exhibit a different behavior than the volume fluxes. Among the 3 runs, B3 has the lowest mean PSW offshore flux, which is consistent with B3 having the highest amount of PSW sinking locally in the polynya water column and the fastest polynya destratification. Interestingly, B4 has the highest mean PSW and density anomaly offshore fluxes, despite the mean offshore volume flux being the lowest. Close examination of the model solution suggests that it results from much of the PSW being trapped in the anticyclonic vortex, which causes some PSW to be carried southward across the alongshore transect back to the source region by the vortex flow (Fig. 8e-f). Trapping of the PSW in the anticyclonic vortex in B4 is caused by wind-induced convergence of surface Ekman flow and then Ekman pumping, i.e., downwelling, at the vortex center. The convergent flow entrains surface waters from the surrounding area toward the vortex center and then carries it downward. This causes water at the vortex center to transition from low density on Day 40 (Fig. 6c-d) to high density on Day 100 (Fig. 8e-f). Essentially, as time proceeds, the downward flow in the vortex center switches from carrying the originally lower-density surface water to carrying

28

544   high-density PSW to the bottom layer. Correspondingly, diagnostics of the horizontal divergence
545   term in the model (not shown) indicate that there is a divergent flow at the vortex bottom (Fig. 6d),
546   presumably resulting from the outward bottom Ekman transport induced by the bottom stress.
547   Ekman pumping of the PSW into the vortex is also consistent with the slower polynya
548   destratification in B4 relative to B3. Entrainment of the PSW into the vortex reduces the amount
549   of PSW sinking in the polynya source region. However, the downwelling flow at the vortex center
550   represents another mechanism of ventilating the bottom layer of the Antarctic continental shelf
551   occurring outside of coastal polynyas. As this study focuses on the water column destratification
552   in the polynya, we leave the influence of the vortex Ekman pumping on the bottom shelf water for
553   future studies.

554   Strong variation of the offshore fluxes in B4 on the time scale of 10–15 days results from
555   instability of the vortex flow that deforms the vortex and then the polynya outflow. Here, we
556   highlight the polynya circulation on two different days, Day 63 and 87, when the offshore fluxes
557   reach a maximum and minimum, respectively (Fig. 16). Modeled solutions on both days show an
558   elongated vortex pattern (Fig. 17). On Day 63, the long axis of the vortex aligns with the cross-
559   shore direction, which gives a large offshore velocity component across the transect. This drives
560   the large offshore volume and PSW transport on that day. On Day 87, the long axis of the elongated
561   vortex is oriented alongshore, parallel to the transect. As a result, the velocity component normal
562   to the transect is weak and fluxes across the transect are minimal. Detailed examination of the B4
563   solution shows that the vortex deformation occurs over much of the water column. It results from
564   the instability of the vortex and causes periodical oscillation in the vortex flow. It generates the
565   10–15-day oscillation of the fluxes in the later part of the simulation (Fig. 16). The time scale of
566   this vortex instability is consistent with the advection time scale of the vortex flow. Given a mean
567   radius of the vortex of ~55 km and a mean flow of 0.3–0.4 m s^{-1}, it takes 10–14 days for the flow
568   to make a complete circle around the vortex. Therefore, the vortex instability likely results from
569   advective resonance of the flow disturbance induced by the fluctuating winds. That is, wind-
570   induced flow disturbances on the time scale of 10–14 days (multiple of the wind periods) are
571   amplified by the recirculation of the disturbance around the vortex. Note that the observed vortex
572   at the TNBP also exhibits deformation on the time scale of several days (Fig. 1c-f). The
573   correspondence between this variation of the polynya circulation and the PSW outflow, and the

574   connection between the outflow and destratification confirm that coastal geometry plays a
575   prominent role in regulating water-column stratification and PSW circulation in a polynya region.

576

Fig. 17. Snapshots of potential density (color) and velocity (arrows) at 100 m depth in Run B4 on Day
63 and Day 87, corresponding to the times of maximum and minimum cross-shore fluxes (Fig. 16b), respectively.
The orange lines in both panels indicate the transect where integrated offshore fluxes are shown in Fig. 16.
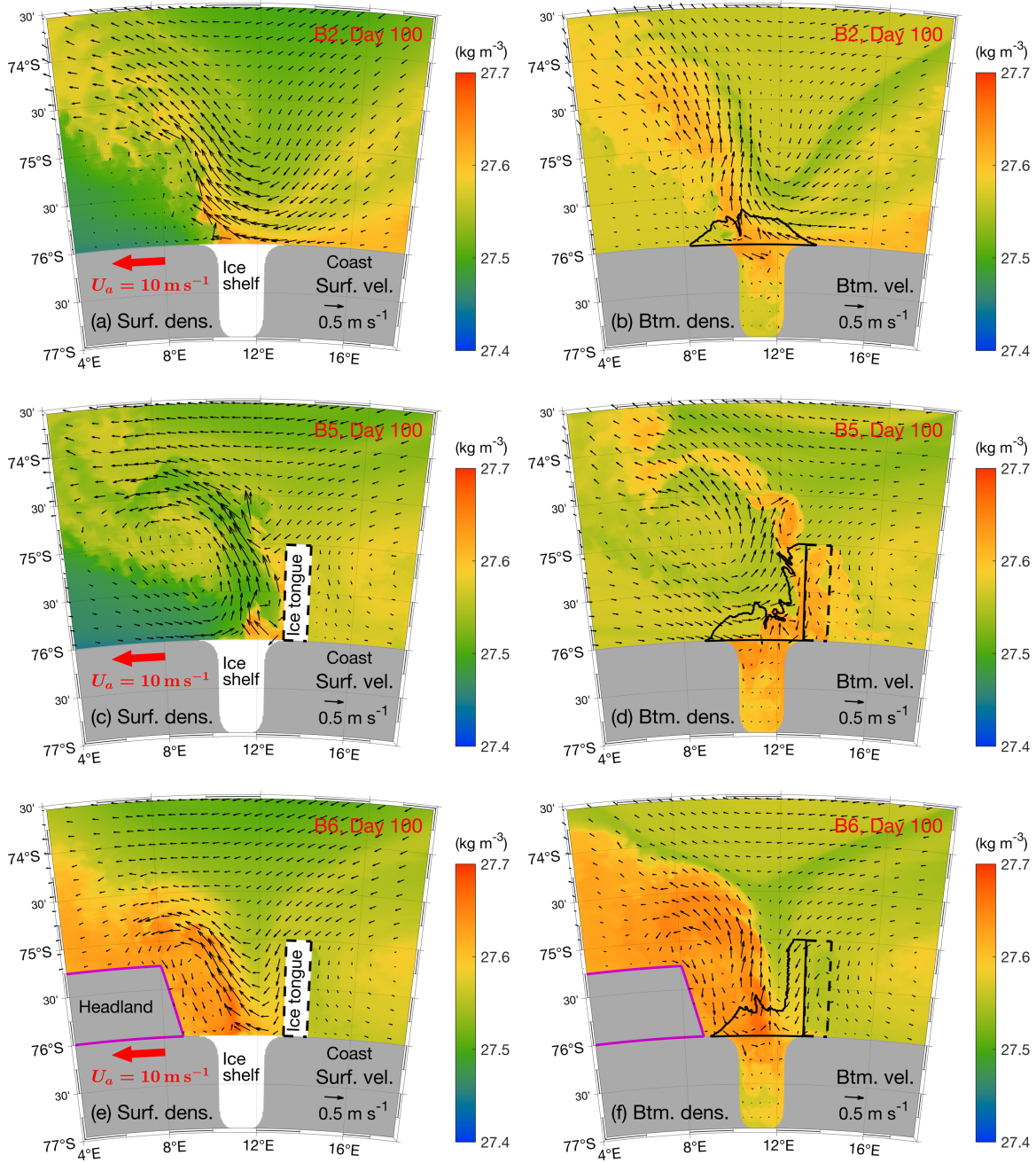
581

4. Discussion

583   With the idealized model setup, we have qualitatively demonstrated the impacts of an ice
584   tongue and a headland on PSW circulation and destratification in polynyas. In the ocean, other
585   physical factors, including those examined in Part I, may interact with coastal geometry and further
586   complicate the polynya circulation. Here, we use alongshore wind as a demonstration. In particular,
587   we examine additional simulations, B2, B5, and B6 (Fig. 18), in which an alongshore easterly wind
588   with a speed of $U_a = 10 \text{ m s}^{-1}$ is added to B1, B3, and B4, respectively. Part I study shows that,
589   without the ice tongue or the headland, alongshore coastal easterly winds U_a can affect polynya
590   destratification through inducing onshore Ekman transport and reducing the offshore export of the
591   PSW. With the ice tongue and the headland, the influence of alongshore winds is qualitatively
592   similar. In particular, on Day 100, modeled surface flows veer westward, and modeled bottom
593   density in the polynya and ice shelf cavity region is higher in B2, B5, and B6, compared to B1,
594   B3, and B4, respectively. Therefore, the Ekman dynamics as explained in Part I is still applicable,
595   and polynya water column destratification is accelerated with the addition of alongshore easterly
596   winds. Meanwhile, bottom densities in the ice shelf cavity in B5 and B6 are also higher than in B2

597   with no ice tongue or headland. This indicates that the influence of the ice tongue and headland on
598   the PSW circulation has not been fundamentally altered by the alongshore easterly winds.

599   The alongshore easterly winds can alter the details of the coastal circulation and affect the
600   overall transport of the PSW. For instance, when an ice tongue and alongshore easterly winds are
601   both present, a polynya is formed in the lee of the ice tongue in both B5 and B6 (Fig. 18d and 18f).
602   In these cases, the ice tongue helps to enhance the sea ice production and PSW formation by
603   expanding the area of the polynya, which is consistent with findings of previous studies (Kurtz
604   and Bromwich 1985; Ohshima et al. 2013; Williams et al. 2010). Runs B5 and B6 also give
605   drastically different density distribution with B6 showing much more PSW being trapped in the
606   larger polynya-vortex region. This indicates that the onshore Ekman transport induced by the
607   easterly winds can interact with the headland to the west of the polynya and efficiently trap much
608   of the PSW in the polynya-vortex region. As a result, the amount of PSW leaving this coastal
609   region is much less in B6 than in B5, resulting in a slightly higher maximum density of PSW at
610   the bottom in B6 than in B5 (Fig. 18d and 18f), whereas the opposite is true in the same geometric
611   setup but without easterly winds (PSW density at the bottom is lower in B4 than in B3; Fig. 8).
612   These suggest that details of the configurations in a coastal polynya have a significant influence
613   and should be considered when studying the dispersal of PSW.

614

Fig. 18. Snapshots of potential density (color) and velocity (arrows) at the surface (left) and bottom (right) on Day 100 from Runs B2 (a-b), B5 (c-d), and B6 (e-f). Black solid lines in (b), (d), and (e) outline the coastal polynya on Day 100.

620   The fundamental processes of coastal geometry affecting polynya circulation and
621 stratification illustrated in this study are applicable not only to the TNBP but also to other coastal
622 polynyas with complex geometry, such as ice tongues and headlands. For instance, the B3-IT
623 simulations with altered ice tongue lengths may be used to explain the significant reduction in
624 DSW export in the Mertz Polynya after its calving event in 2010 (Lacarra et al. 2014; Snow et al.
625 2018). Assuming that the Mertz Glacier Tongue keeps a growth rate of ~1 km per year (Giles
626 2017) and the offshore width of the Mertz Polynya is ~40 km similar to our modeled polynya, the
627 restoration of DSW export from the Mertz Polynya to a level comparable to that prior to its 2010
628 calving event shall be expected within ~40 years, when the Mertz Glacier Tongue exceeds the
629 offshore width of the Mertz Polynya. Moreover, the case with the ice tongue and alongshore
630 easterly winds (B5) can qualitatively represent Cape Darnley Polynya, where coastal easterly
631 winds are prominent and the sea ice inflow from the east has been blocked by a grounded iceberg
632 (Nihashi and Ohshima 2015; Ohshima et al. 2013). Consistently, through analyzing wintertime
633 hydrographic measurements in the Cape Darnley Polynya in 2017, Aoki et al. (2020) suggested
634 that local three-dimensional DSW circulation might affect salinity evolution in the polynya water
635 column.

636   The processes described here may explain differences in DSW formation among Antarctic
637 coastal polynyas. For instance, the coastal polynyas that are known to be sources of the DSW and
638 AABW, such as the TNBP, the Mertz Polynya, the Vincennes Bay Polynya, and the Cape Darnley
639 Polynya (Budillon and Spezie 2000; Kitade et al. 2014; Ohshima et al. 2013; Rusciano et al. 2013;
640 Williams et al. 2010), are often affiliated with ice tongues or similar features. Presumably, the
641 neighboring ice tongues or icebergs enhance local sinking of the PSW in the polynyas and facilitate
642 formation of the DSW, which then flows offshore, supplying AABW.

643

644 **5. Summary**

645   This study shows that coastal geometry can substantially affect the destratification rate in
646 coastal polynyas. Even with the same polynya size and the same rate of PSW production at the
647 polynya surface, the coastal circulation and water column destratification processes vary
648 significantly across simulations with and without an ice tongue or a headland (Section 3; Figs. 8,
649 9, and 10). Besides impeding sea ice flow into the polynya at the ocean surface, an ice tongue can

650 block water column circulation on one side of the polynya and cause the polynya outflow to abut

651 the ice shelf (Fig. 5). This creates a relatively stagnant wedge region at the corner between the ice

652 shelf and the ice tongue, which reduces offshore loss of the PSW, enhances local sinking of the

653 PSW in the polynya, and then accelerates the destratification of the polynya water column. A

654 headland on the other side of the polynya can also alter the three-dimensional PSW dispersal by

655 restoring the alongshore symmetry of the polynya circulation (Fig. 6). The headland causes the

656 polynya outflow to separate from the ice tongue and allows ambient water to flow along the ice

657 tongue to compensate for the polynya outflow. This process enhances the offshore transport of the

658 PSW and slows down polynya water-column destratification. Meanwhile, simulations with

659 different ice tongue lengths demonstrate that the ice tongue's blocking effect is only effective when

660 the ice tongue is longer than the cross-shore width of the polynya (Fig. 14). Adding the headland

661 to the other side of the polynya generates an intense vortex (Fig. 13f), which resembles

662 observations in the TNBP (Fig. 1c-h). Instability of the vortex flow drives strong temporal

663 variability in the polynya outflow, which affects the export of PSW from the polynya region and

664 polynya destratification (Figs. 16 and 17). All these results indicate the importance of considering

665 small-scale icescape and coastline geometry in studies of polynya stratification and PSW

666 circulation.

667   Part I of this study shows that alongshore easterly winds can suppress offshore transport of

668 PSW and enhance polynya destratification through onshore Ekman transport. This Part II work

669 further demonstrates that besides the circulation barrier induced by the winds in Part I, physical

670 barrier such as neighboring ice tongue can also modify the circulation and accelerate water column

671 destratification in the polynya. Together, these studies highlight the impacts of a variety of physical

672 factors, such as wind strength, wind direction, air temperature, initial ambient stratification, water

673 depth, ice tongues, and coastal geometry on polynya water column destratification. The influences

674 of other factors remain to be explored, e.g., land-fast ice, bathymetric variations, onshore intrusion

675 of the offshore warm Circumpolar Deep Water, ice shelf melting, and shape and location of the

676 continental shelf. In addition, variations of the polynya stratification due to changes in factors such

677 as breaking of the ice tongue and land-fast ice and the associated relocation or size change of the

678 polynyas also need to be investigated in future studies.

679   Despite these limitations, we have demonstrated with high-resolution idealized numerical

680 models that altering local forcing and geometric features such as ice tongues can modify the

681   polynya circulation and lead to substantial changes in the rate of polynya destratification and
682   pathways of the PSW dispersal. Only when a polynya water column is completely mixed, part of
683   the PSW formed on the polynya surface can sink directly down to the bottom and become DSW,
684   which then propagates offshore on the seafloor across the shelf edge supplying AABW. Because
685   the winter season has a limited length and the water column tends to re-stratify in the summer, the
686   time it takes the polynya water column to be completely mixed determines whether a polynya can
687   form DSW and supply AABW. Hence, the rate of destratification studied here is essential for
688   determining the amount of DSW formed in a particular polynya and then exported to the deep
689   ocean supplying AABW. Understanding impacts of the physical factors in a coastal region on the
690   PSW circulation and destratification in polynyas is vital to understanding the AABW formation
691   and global ocean water mass distribution. For instance, the presence of alongshore easterly winds
692   and an ice tongue at a polynya would increase the amount of DSW formed in the polynya to supply
693   AABW. Future modeling studies of the large-scale AABW formation should either resolve or
694   parameterize these local influences.

695

699

700   *Data Availability Statement.*

701   The MODIS image was obtained from the Worldview tool from NASA's Earth Observing
702   System Data and Information System at https://worldview.earthdata.nasa.gov/. The Sentinel-1
703   image processed by ESA was downloaded from NASA's Distributed Active Archive Centers
704   operated by the Alaska Satellite Facility at https://asf.alaska.edu/. The meteorological station data
705   were downloaded from the University of Wisconsin-Madison Automatic Weather Station Program
706   at https://amrc.ssec.wisc.edu/. The PIPERS CTD data were obtained from the U.S. Antarctic
707   Program Data Center at https://www.usap-dc.org/view/dataset/601422. The model code and
708   scripts used to conduct the simulations and analyses in this study are available at
709   https://doi.org/10.5281/zenodo.7761706.

710

711 REFERENCES

712 Ackley, S. F., and Coauthors, 2020: Sea-ice production and air/ice/ocean/biogeochemistry
713   interactions in the Ross Sea during the PIPERS 2017 autumn field campaign. *Ann. Glaciol.*,
714   **61**, 181–195, https://doi.org/10.1017/aog.2020.31.

715 Aoki, S., K. Ono, D. Hirano, and T. Tamura, 2020: Continuous winter oceanic profiling in the
716   Cape Darnley Polynya, East Antarctica. *J. Oceanogr.*, **76**, 365–372,
717   https://doi.org/10.1007/s10872-020-00550-w.

718 Bromwich, D. H., 1989: Satellite analyses of Antarctic katabatic wind behavior. *Bull. - Am.*
719   *Meteorol.   Soc.*,   **70**,   738–749,   https://doi.org/10.1175/1520-
720   0477(1989)070<0738:SAOAKW>2.0.CO;2.

721 Bromwich, D. H., and D. D. Kurtz, 1984: Katabatic wind forcing of the Terra Nova Bay polynya.
722   *J. Geophys. Res.*, **89**, 3561, https://doi.org/10.1029/JC089iC03p03561.

723 Budillon, G., and G. Spezie, 2000: Thermohaline structure and variability in the Terra Nova Bay
724   polynya, Ross Sea. *Antarct. Sci.*, **12**, 493–508, https://doi.org/10.1017/s0954102000000572.

725 Dinniman, M. S., P. St-Laurent, K. R. Arrigo, E. E. Hofmann, and G. L. van Dijken, 2020: Analysis
726   of Iron Sources in Antarctic Continental Shelf Waters. *J. Geophys. Res. Ocean.*, **125**, 1–19,
727   https://doi.org/10.1029/2019JC015736.

728 Frezzotti, M., and M. C. G. Mabin, 1994: 20th century behaviour of Drygalski Ice Tongue, Ross
729   Sea, Antarctica. *Ann. Glaciol.*, **20**, 397–400, https://doi.org/10.1017/S026030550001675X.

730 Giles, A. B., 2017: The Mertz Glacier Tongue, East Antarctica. Changes in the past 100 years and
731   its cyclic nature - Past, present and future. *Remote Sens. Environ.*, **191**, 30–37,
732   https://doi.org/10.1016/j.rse.2017.01.003.

733 Guest, P. S., 2021: Inside Katabatic Winds Over the Terra Nova Bay Polynya: 2. Dynamic and
734   Thermodynamic   Analyses.   *J.   Geophys.   Res.   Atmos.*,   **126**,
735   https://doi.org/10.1029/2021JD034904.

736   Indrigo, C., C. F. Dow, J. S. Greenbaum, and M. Morlighem, 2020: Drygalski Ice Tongue stability

737   influenced   by   rift   formation   and   ice   morphology.   *J.   Glaciol.*,

738   https://doi.org/10.1017/jog.2020.99.

739   Kitade, Y., and Coauthors, 2014: Antarctic bottom water production from the Vincennes Bay

740   Polynya,   East   Antarctica.   *Geophys.   Res.   Lett.*,   **41**,   3528–3534,

741   https://doi.org/10.1002/2014GL059971.

742   Kurtz, D. D., and D. H. Bromwich, 1985: A recurring, atmospherically forced polynya in Terra

743   Nova Bay. *Antarctic Research Series*, Vol. 43 of, 177–201.

744   Lacarra, M., M.-N. Houssais, C. Herbaut, E. Sultan, and M. Beauverger, 2014: Dense shelf water

745   production in the Adélie Depression, East Antarctica, 2004-2012: Impact of the Mertz Glacier

746   calving. *J. Geophys. Res. Ocean.*, **119**, 5203–5220, https://doi.org/10.1002/2013JC009124.

747   Le Bel, D. A., C. J. Zappa, G. Budillon, and A. L. Gordon, 2021: Salinity response to atmospheric

748   forcing   of   the   Terra   Nova   Bay   polynya,   Antarctica.   *Antarct.   Sci.*,   **14**,   1–14,

749   https://doi.org/10.1017/S0954102021000146.

750   Marshall, J., A. Adcroft, C. Hill, L. Perelman, and C. Heisey, 1997: A finite-volume,

751   incompressible navier stokes model for, studies of the ocean on parallel computers. *J.*

752   *Geophys. Res. C Ocean.*, **102**, 5753–5766, https://doi.org/10.1029/96JC02775.

753   Massom, R. A., P. T. Harris, K. J. Michael, and M. J. Potter, 1998: The distribution and formative

754   processes of latent-heat polynyas in East Antarctica. *Ann. Glaciol.*, **27**, 420–426,

755   https://doi.org/10.3189/1998AoG27-1-420-426.

756   Massom, R. A., K. L. Hill, V. I. Lytle, A. P. Worby, M. J. Paget, and I. Allison, 2001: Effects of

757   regional fast-ice and iceberg distributions on the behaviour of the Mertz Glacier polynya, East

758   Antarctica. *Ann. Glaciol.*, **33**, 391–398, https://doi.org/10.3189/172756401781818518.

759   Morales Maqueda, M. A., A. J. Willmott, and N. R. T. Biggs, 2004: Polynya dynamics: A review

760   of observations and modeling. *Rev. Geophys.*, **42**, https://doi.org/10.1029/2002RG000116.

761   Nihashi, S., and K. I. Ohshima, 2015: Circumpolar Mapping of Antarctic Coastal Polynyas and

762   Landfast   Sea   Ice: Relationship   and   Variability.   *J.   Clim.*,   **28**,   3650–3670,

763   https://doi.org/10.1175/JCLI-D-14-00369.1.

764   Ohshima, K. I., and Coauthors, 2013: Antarctic Bottom Water production by intense sea-ice

765   formation in the Cape Darnley polynya. *Nat. Geosci.*, **6**, 235–240,

766   https://doi.org/10.1038/ngeo1738.

767   Parmiggiani, F., and C. Fragiacomo, 2005: Cover: The calving event of the Drygalski Ice Tongue

768   of February 2005. *Int. J. Remote Sens.*, **26**, 4633–4638,

769   https://doi.org/10.1080/01431160500238828.

770   Randall-Goodwin, E., and Coauthors, 2015: Freshwater distributions and water mass structure in

771   the Amundsen Sea Polynya region, Antarctica. *Elem. Sci. Anthr.*, **3**, 1–22,

772   https://doi.org/10.12952/journal.elementa.000065.

773   Rusciano, E., G. Budillon, G. Fusco, and G. Spezie, 2013: Evidence of atmosphere-sea ice-ocean

774   coupling in the Terra Nova Bay polynya (Ross Sea-Antarctica). *Cont. Shelf Res.*, **61**–**62**, 112–

775   124, https://doi.org/10.1016/j.csr.2013.04.002.

776   Silvano, A., S. R. Rintoul, B. Peña-Molino, W. R. Hobbs, E. Van Wijk, S. Aoki, T. Tamura, and

777   G. D. Williams, 2018: Freshening by glacial meltwater enhances melting of ice shelves and

778   reduces formation of Antarctic Bottom Water. *Sci. Adv.*, **4**,

779   https://doi.org/10.1126/sciadv.aap9467.

780   Snow, K., S. R. Rintoul, B. M. Sloyan, and A. M. C. Hogg, 2018: Change in Dense Shelf Water

781   and Adélie Land Bottom Water Precipitated by Iceberg Calving. *Geophys. Res. Lett.*, **45**,

782   2380–2387, https://doi.org/10.1002/2017GL076195.

783   Stevens, C., W. Sang Lee, G. Fusco, S. Yun, B. Grant, N. Robinson, and C. Y. Hwang, 2017: The

784   influence of the Drygalski Ice Tongue on the local ocean. *Ann. Glaciol.*, **58**, 51–59,

785   https://doi.org/10.1017/aog.2017.4.

786   Tamura, T., G. D. Williams, A. D. Fraser, and K. I. Ohshima, 2012: Potential regime shift in

787   decreased sea ice production after the Mertz Glacier calving. *Nat. Commun.*, **3**,

788   https://doi.org/10.1038/ncomms1820.

789   Thompson, L., M. Smith, J. Thomson, S. Stammerjohn, S. Ackley, and B. Loose, 2020: Frazil ice

790   growth and production during katabatic wind events in the Ross Sea, Antarctica. *Cryosph.*,

791   **14**, 3329–3347, https://doi.org/10.5194/tc-14-3329-2020.

792   Wenta, M., and J. J. Cassano, 2020: The Atmospheric Boundary Layer and Surface Conditions
793   during Katabatic Wind Events over the Terra Nova Bay Polynya. *Remote Sens.*, **12**, 4160,
794   https://doi.org/10.3390/rs12244160.

795   Williams, G. D., S. Aoki, S. S. Jacobs, S. R. Rintoul, T. Tamura, and N. L. Bindoff, 2010: Antarctic
796   bottom water from the adélie and George v Land Coast, East Antarctica (140-149°E). *J.*
797   *Geophys. Res. Ocean.*, **115**, 1–29, https://doi.org/10.1029/2009JC005812.

798   Xu, Y., W. G. Zhang, T. Maksym, R. Ji, and Y. Li, 2023: Stratification Breakdown in Antarctic
799   Coastal Polynyas, Part I: Influence of Physical Factors on the Destratification Timescale,
800   submitted.

801   Yoon, S.-T., and Coauthors, 2020: Variability in high-salinity shelf water production in the Terra
802   Nova Bay polynya, Antarctica. *Ocean Sci.*, **16**, 373–388, https://doi.org/10.5194/os-16-373-
803   2020.

804